AD________________

Award Number: W81XWH-10-1-0132

TITLE: Metallated DNA Aptamers for Prostate Cancer Treatment

PRINCIPAL INVESTIGATOR: William H. Gmeiner

CONTRACTING ORGANIZATION: Wake Forest University , Winston-Salem, NC 27157

REPORT DATE: October 2013

TYPE OF REPORT: Revised Final Addendum

PREPARED FOR: U.S. Army Medical Research and Materiel Command
Fort Detrick, Maryland 21702-5012

DISTRIBUTION STATEMENT: Approved for Public Release;
Distribution Unlimited

REPORT DOCUMENTATION PAGE	*Form Approved* *OMB No. 0704-0188*

1. REPORT DATE October 2013	**2. REPORT TYPE** Revised First Addendum	**3. DATES COVERED** 15 Feb 2010 - 14 Sep 2013
4. TITLE AND SUBTITLE Metallated DNA Aptamers for Prostate Cancer Treatment		**5a. CONTRACT NUMBER**
		5b. GRANT NUMBER W81XWH-10-1-0132
		5c. PROGRAM ELEMENT NUMBER
6. AUTHOR(S) William H. Gmeiner		**5d. PROJECT NUMBER**
		5e. TASK NUMBER
E-Mail: bgmeiner@wakehealth.edu		**5f. WORK UNIT NUMBER**
7. PERFORMING ORGANIZATION NAME(S) AND ADDRESS(ES) Wake Forest University, Winston-Salem, NC 27157		**8. PERFORMING ORGANIZATION REPORT NUMBER**
9. SPONSORING / MONITORING AGENCY NAME(S) AND ADDRESS(ES) U.S. Army Medical Research and Materiel Command Fort Detrick, Maryland 21702-5012		**10. SPONSOR/MONITOR'S ACRONYM(S)**
		11. SPONSOR/MONITOR'S REPORT NUMBER(S)

12. DISTRIBUTION / AVAILABILITY STATEMENT

Approved for Public Release; Distribution Unlimited

13. SUPPLEMENTARY NOTES

14. ABSTRACT

The purpose of this project is to develop DNA aptamer complexes that are selectively cytotoxic to PSMA+ prostate cancer (PCa) cells. Our studies showed Zn2+ is cytotoxic to prostate cancer cells and also sensitizes PCa cells to chemotherapy. We developed a new DNA motif for Zn2+ delivery. We also developed a new chemical strategy for delivering the cytotoxic drug doxorubicin to cancer cells. We have demonstrated that our novel dimeric aptamer complexes are selectively internalized by PSMA+ prostate cancer cells and have demonstrated selective cytotoxicity with delivery of doxorubicin. We also developed a new nanoparticle (NP) composed of porphyrin and DNA and demonstrated that this NP was cytotoxic to bladder cancer cells in vitro, was non-toxic in vivo, and displayed strong anti-tumor activity in vivo. The aptamer complexes and the NPs we developed in this project are highly selective and highly active agents that have the potential to markedly improve chemotherapy for treatment of advanced prostate cancer. We developed a new process for selective release of doxorubicin from a DNA scaffold in tumor cells and completed analysis of F10 anti-tumor activity in prostate cancer xenografts.

15. SUBJECT TERMS

Prostate cancer, DNA-metal interactions, Zn2+, structural biology

16. SECURITY CLASSIFICATION OF:			**17. LIMITATION OF ABSTRACT**	**18. NUMBER OF PAGES**	**19a. NAME OF RESPONSIBLE PERSON** USAMRMC
a. REPORT U	**b. ABSTRACT** U	**c. THIS PAGE** U	UU	53	**19b. TELEPHONE NUMBER** *(include area code)*

Table of Contents

Aim 3: ***Evaluate the safety and anti-tumor activity of chelated-Zn^{2+} in combination with advanced FPs as well as metallated DNA aptamer complexes that include both chelated Zn^{2+} and FdU.***

Task 3.A. Evaluate the safety of FdUMP[10] in combination with ZnPc.

Our experiments with the porphyrin ZnPc binding to DNA resulted in studies with the porphyrin meso-tetra-4-pyridyl porphine (MTP) interacting with single-stranded DNA (ssDNA). As F10 is expensive (> $3,000/g) we used another ssDNA sequence (dGT(20)) in these studies.

We demonstrated formation of discrete nanoparticles (NPs) (Figure S1).

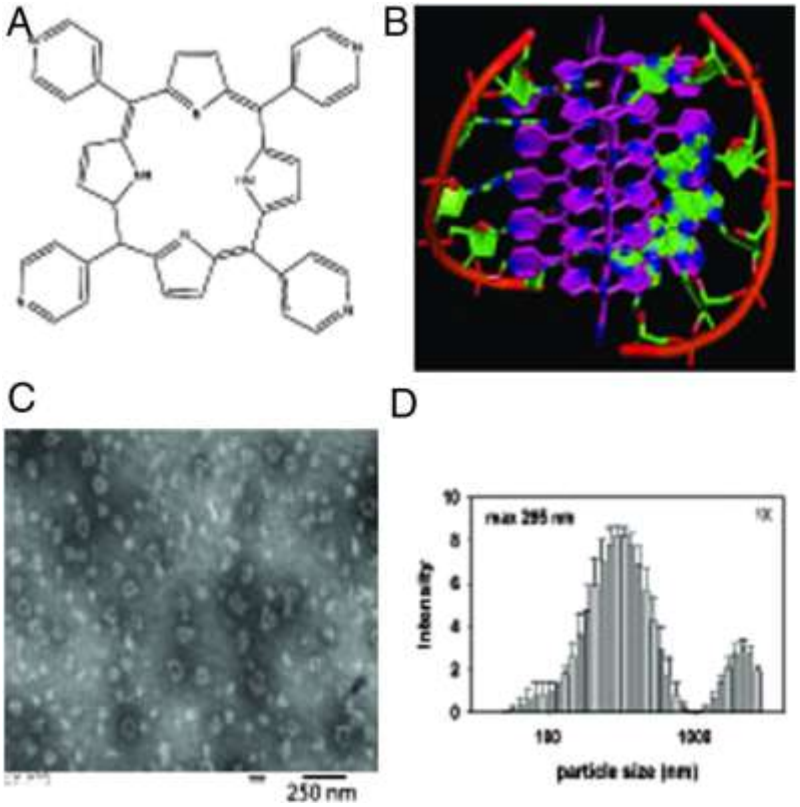

Figure S1. Discrete porphyrin:DNA nanoparticles (PDN) form upon sonication of MTP porphyrin with ssDNA. (A) Structure of the MTP porphyrin used for these studies. (B) Molecular model of PDN nanocomplex showing both porphyrin-porphyrin and porphyrin:DNA interactions. (C) transmission electron micrograph (TEM) image of PDN nanoparticles. (D) Dynamic light scattering (DLS) analysis of PDN hydrodynamic radius distribution.

We evaluated the safety of the MTP-containing PDN in vivo performing intratumoral injections of the PDN in nude mice. The PDN-treated group displayed no adverse effects due to treatment demonstrating the safety of the nanoparticle *in vivo*. These data were included in our publication “Non-covalent assembly of meso-tetra-pyridyl porphine…” which is included as **Appendix #1** of this revised report. We also completed analysis of the safety of FdUMP[10] in vivo which we established is safe and in fact much better tolerated than 5-FU *in vivo*. These data are included in our manuscript “F10 inhibits growth of PC3 xenografts…” which is included as **Appendix #2** of this revised report.

Task 3.B. Evaluate the efficacy of FdUMP[10] in combination with ZnPc. We evaluated the efficacy of PDN prepared with the single-stranded DNA d(GT)20. We established that PDN display significant and light-dependent anti-tumor activity (Figure S2). These data were included in our publication "Non-covalent assembly of meso-tetra-

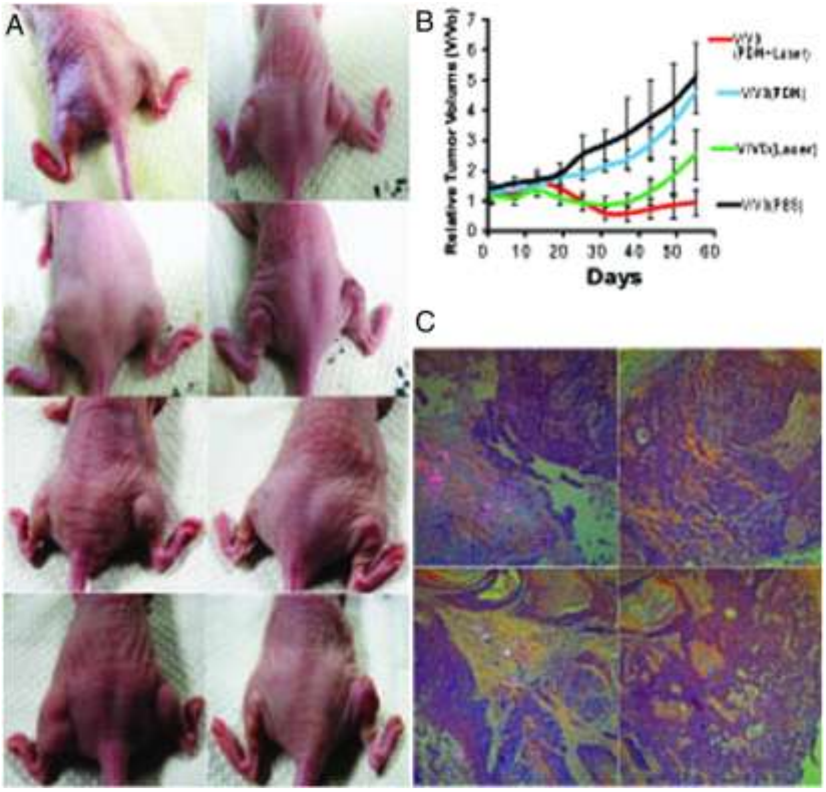

Figure S2. PDN/light treatment displays significant anti-tumor activity in vivo. (A) Representative tumors from the four treatment groups at day 0 (top row – prior to any treatment), day 1 (2nd row – after initial treatments), day 25 (3rd row – at the conclusion of light treatment), and day 55 (bottom row – end of study). The left mouse, left flank (L, L) received no treatment; the left mouse, right flank (L-R) received PDN-only. The right mouse, left flank (R, L) received PDN/light and the right mouse, right flank (R, R) received light-only. (B) Plot of relative volumes for bladder cancer xenografts over time following treatment with PDN/light (red), light-only (green), PDN-only (blue), no treatment (black). (C) Histopathological analysis of tumor tissue. Polarization detection as part of histological analysis for PDN in tissues excised from animals at the conclusion of the study receiving the following treatments: (top-left) – PDN/light; (top-right) – lightonly; (bottom-left) – PDN-only; (bottom-right) – no treatment.

We also completed analysis of efficacy data for FdUMP[10] towards PC3 xenografts alone and in combination with radiation. These data are included in our manuscript "F10 inhibits growth of PC3 xenografts…" which is included as Appendix #2 of this revised report.

Task 3.C. Evaluate the safety of Dimeric Aptamer Complexes. We completed a study in which we evaluated the safety of the dimeric aptamer complex following intravenous administration. In this study we attached the dimeric aptamer complex to a liposome. No toxicity was observed.

We completed studies with the DNA hairpins that we have previously used to deliver Zn2+ and FdU nucleotides and discovered a unique covalent linkage that we used for delivery of doxorubicin. We published these findings in Bioconjugate Chemistry (Appendix #3).

KEY RESEARCH ACCOMPLISHMENTS:

- We completed safety studies establishing PDN are safe upon intra-tumoral administration.
- We completed analysis of data demonstrating FdUMP[10] is safe upon intravenous administration.
- We completed efficacy studies demonstrating PDN display anti-tumor activity that is light-dependent.
- We completed analysis of data demonstrating FdUMP[10] is efficacious and radiosensitizing upon intravenous administration.
- We performed studies demonstrating that dimeric aptamer complexes are safe upon intravenous administration.
- We completed studies demonstrating the DNA hairpin could be used for formation of covalent complexes of doxorubicin that are useful for targeted drug delivery.

REPORTABLE OUTCOMES:

Ghosh S, Ucer KB, D'Agostino R Jr, Grant K, Sirintrapun J, Thomas MJ, Hantgan R, Bharadwaj M, **Gmeiner WH**. Non-covalent assembly of meso-tetra-4-pyridyl porphine with single-stranded DNA to form nano-sized complexes with hydrophobicity-dependent DNA release and anti-tumor activity. Nanomedicine NBM 2014; 10: 451-461.
http://www.sciencedirect.com/science/article/pii/S154996341300364X

Appendix #1

William H. Gmeiner[1*], Mark C. Willingham[2], J. Daniel Bourland[3], Heather C. Hatcher[1], Thomas L. Smith[4], Ralph B. D'Agostino Jr.[5], William Blackstock[3] F10 Inhibits Growth of PC3 Xenografts and Enhances the Effects of Radiation Therapy. JSM Clin Oncol Res 2(4):1028.
Appendix#2

Stuart CH, Horita DA, Thomas MJ, Salsbury Jr FR, Lively, MO, Gmeiner WH. Site-specific DNA-doxorubicin conjugates display enhanced cytotoxicity to breast cancer cells. Bioconj. Chem. 2014. In Press.
http://www.ncbi.nlm.nih.gov/pubmed/24450459
Appendix #3

Conclusion: Additional progress was made towards completing the objectives outlined for the no-cost extension. All project goals have been addressed.

References:

Ghosh S, Ucer KB, D'Agostino R Jr, Grant K, Sirintrapun J, Thomas MJ, Hantgan R, Bharadwaj M, **Gmeiner WH**. Non-covalent assembly of meso-tetra-4-pyridyl porphine with single-stranded DNA to form nano-sized complexes with hydrophobicity-dependent DNA release and anti-tumor activity. Nanomedicine NBM 2014; 10: 451-461.
http://www.sciencedirect.com/science/article/pii/S154996341300364X

William H. Gmeiner[1*], Mark C. Willingham[2], J. Daniel Bourland[3], Heather C. Hatcher[1], Thomas L. Smith[4], Ralph B. D'Agostino Jr.[5], William Blackstock[3] F10 Inhibits Growth of PC3 Xenografts and Enhances the Effects of Radiation Therapy. JSM Clin Oncol Res 2(4):1028.

Stuart CH, Horita DA, Thomas MJ, Salsbury Jr FR, Lively, MO, Gmeiner WH. Site-specific DNA-doxorubicin conjugates display enhanced cytotoxicity to breast cancer cells. Bioconj. Chem. 2014. In Press.
http://www.ncbi.nlm.nih.gov/pubmed/24450459

Nanomedicine: Nanotechnology, Biology, and Medicine
xx (2013) xxx – xxx

nanomedjournal.com

Non-covalent assembly of meso-tetra-4-pyridyl porphine with single-stranded DNA to form nano-sized complexes with hydrophobicity-dependent DNA release and anti-tumor activity

Supratim Ghosh, PhD[a,b], Kamil B. Ucer, PhD[g], Ralph D'Agostino, Jr., PhD[f], Ken Grant, BS[c], Joseph Sirintrapun, MD[c], Michael J. Thomas, PhD[d], Roy Hantgan, PhD[d], Manish Bharadwaj, PhD[e], William H. Gmeiner, PhD, MBA[a,b,f,*]

[a]*Program in Molecular Genetics, Wake Forest School of Medicine, Winston-Salem, NC, USA*
[b]*Department of Cancer Biology, Wake Forest School of Medicine, Winston-Salem, NC, USA*
[c]*Department of Pathology, Wake Forest School of Medicine, Winston-Salem, NC, USA*
[d]*Department of Biochemistry, Wake Forest School of Medicine, Winston-Salem, NC, USA*
[e]*Department of Genrontology, Wake Forest School of Medicine, Winston-Salem, NC, USA*
[f]*Comprehensive Cancer Center, Wake Forest School of Medicine, Winston-Salem, NC, USA*
[g]*Department of Physics, Wake Forest University, Winston-Salem, NC, USA*

Received 28 June 2013; accepted 22 July 2013

Abstract

DNA and porphyrin based therapeutics are important for anti-cancer treatment. The present studies demonstrate single-stranded DNA (ssDNA) assembles with meso-tetra-4-pyridyl porphine (MTP) forming porphyrin:DNA nano-complexes (PDN) that are stable in aqueous solution under physiologically relevant conditions and undergo dissociation with DNA release in hydrophobic environments, including cell membranes. PDN formation is DNA-dependent with the ratio of porphyrin:DNA being approximately two DNA nucleobases per porphyrin. PDN produce reactive oxygen species (ROS) in a light-dependent manner under conditions that favor nano-complex dissociation in the presence of hydrophobic solvents. PDN induce light-dependent cytotoxicity *in vitro* and anti-tumor activity towards bladder cancer xenografts *in vivo*. Light-dependent, PDN-mediated cell death results from ROS-mediated localized membrane damage due to lipid peroxidation with mass spectrometry indicating the generation of the lipid peroxidation products 9- and 13-hydroxy octadecanoic acid. Our results demonstrate that PDN have properties useful for therapeutic applications, including cancer treatment.

Key words: Multi-modality nanoparticle; Cancer therapy; Photodynamic therapy; Porphyrin: DNA assembly

Background

Porphyrins are a group of compounds containing the porphin ring structure that is important in biology and medicine and that has recently been studied for their propensity to form nanomaterials,[1,2] including nanotubes[3] through non-covalent chemistry. The principal driving force for porphyrin self-assembly is hydrophobic interactions[4] resulting in vertical stacking of porphyrins in aqueous solutions in a pH-dependent manner.[5,6] Previous studies demonstrating nanoparticle assembly of porphyrins were conducted in pure water and self-assembly was optimal at acidic pH, limiting potential biological applications.[5,6] Porphyrin assembly has been shown to be modulated by biological molecules, such as poly-glutamic acid,[7] however these complexes also have limited stability under physiologically relevant conditions. The preparation of porphyrin-containing nanostructures that are stable under biologically relevant conditions, but that dissociate in a predicable manner could be useful for drug delivery, photodynamic therapy (PDT),[8–12] and other biologically relevant processes.[13]

Funding Resources: This work was supported by DOD PCRP 093606 (WHG) and NIH-NCI P30CA012197 (WHG).

*Corresponding author: Department of Cancer Biology, Wake Forest School of Medicine, Winston-Salem, NC 27157, USA.
E-mail address: bgmeiner@wakehealth.edu (W.H. Gmeiner).

1549-9634/$ – see front matter © 2013 Elsevier Inc. All rights reserved.
http://dx.doi.org/10.1016/j.nano.2013.07.019

Please cite this article as: Ghosh S., et al., Non-covalent assembly of meso-tetra-4-pyridyl porphine with single-stranded DNA to form nano-sized complexes with hydrophobicity-dependent.... *Nanomedicine: NBM* 2013;xx:1-11, http://dx.doi.org/10.1016/j.nano.2013.07.019

The present studies focus on developing porphyrin:DNA nanoparticles (PDN) that are stable under physiological conditions of pH, salt, and temperature and that have potential use for PDT as well as in nucleic acid delivery. In principle, hydrophobic stacking and hydrogen bonding interactions between appropriately modified porphyrins and DNA (or RNA) nucleobases could provide an additional interaction complementary to porphyrin aggregation potentially resulting in production of porphyrin:DNA nanoparticles (PDN) that have both the light-mediated cell killing properties of porphyrin photosensitizers (PS) and the capacity to deliver a nucleic acid payload with therapeutic utility. Our studies utilize meso-tetra-4-pyridyl porphin (MTP) interacting with the single-stranded DNA (ssDNA) $(GT)_{20}$. In the absence of DNA, MTP forms amorphous aggregates in aqueous solution under physiological conditions, although acidification of the solution ($<$pH 3.0) dissociates the aggregates and re-generates non-complexed porphyrin. The pyridyl groups of MTP have the potential to base stack and/or form hydrogen bonds with nucleobases of DNA at physiological pH and the phosphodiester backbone of DNA may confer aqueous solubility to the complex. We demonstrate that unlike previous porphyrin:DNA complexes,[14–18] the PDN developed with this approach form discrete porphyrin:DNA nanoparticles that are of the appropriate size for drug-delivery applications via the enhanced permeability and retention (EPR) effect[19,20] and that readily dissociate upon cell internalization to deliver a therapeutic payload.

The PDN prepared by self-assembly of MTP and ssDNA have the potential to be highly effective agents for cancer treatment. We demonstrate that PDN are capable of exerting light-dependent cytotoxicity towards bladder cancer cells both in tissue culture models and *in vivo*. The light-dependent cytotoxicity of PDN occurs with generation of the lipid oxidation products 9- and 13-hydroxy octadecanoic acid (HODE) and with damage to the integrity of the plasma membrane consistent with generation of singlet oxygen via a type II photochemical reaction.[21] PDN initially associate with the plasma membrane and are internalized into endocytic vesicles where free DNA and porphyrin may release, recovering the functionality of the constituent materials while leaving no extraneous carrier that may impart systemic toxicities. Importantly, localized PDN-treatment combined with light-activation significantly reduced tumor volumes *in vivo*.

Methods

Preparation of porphyrin:DNA nanoparticles

Meso-tetra-4-pyridyl porphine (MTP; ~0.25 mg – Frontier Scientific) was suspended in 5 mL 20 mM Phosphate Buffer (pH 7.4) containing 5 nmol (0.025 mg/mL) $d(GT)_{20}$ and sonicated in a bath sonicator for 1.5 h with temperature maintained at 5-7 °C. A second addition of MTP (~0.25 mg) was followed by an additional 1 h sonication, followed by addition of 5 nmol DNA and further sonication for 1 h. The mixture was then centrifuged and filtered with membrane filter tube (Amicon Ultra, MWCO 100 KDa) to remove any free DNA. The resulting brownish-yellow aqueous suspension was used for subsequent studies. The porphyrin:DNA ratio for PDN (~19:1) was calculated by acid dissolution of the nanoparticle followed by spectrophotometric determination.

Biophysical characterization of PDN

UV-Vis spectra were collected under ambient conditions using a DU800 UV-Vis spectrophotometer (Beckman Coulter). Fluorescence spectra were acquired using a Perkin-Elmer-F1000 fluorometer with excitation at 420 nm and emission scanned over the range 550-900 nm. Transmission electron microscopy (TEM) images of PDN were acquired using a FEI Thcnai-Spirit TEM. TEM images were analyzed and the distribution of PDN length and diameter was determined using Matlab software. Dynamic light scattering (DLS) was performed under ambient conditions using a Malvern Zetasizer nano series ZEN-1600 in particle size and measurement mode. Each sample was read for 60 s using a 442.0 Kcps count rate. Data were analyzed using Malvern software.

Hydrophobicity-dependent DNA release and endosomal uptake of PDN

PDN were prepared as a suspension in 20 mM phosphate buffer (250 μg/mL) which was then diluted to 15 μg/mL in 20 mM phosphate buffer mixture containing either 0%, 20% or 40% acetonitrile. The desired pH was obtained by adding concentrated HCl or NaOH. The pH of all mixtures was further confirmed using a pH meter after addition of all components. After addition of all components, mixtures were incubated at room temperature overnight followed by filtration through membrane filter tubes (Amicon Ultra; 100KDa MWCO). 25 μL of each filtrate including a 2.5 μM $d(GT)_{20}$ standard was then analyzed by polyacrylamide gel electrophoresis (15% native gel in TBE buffer, pH 7.4, 50 mA for 90 min). The gel was stained using Syber Gold solution and scanned using a Typhoon FLA 9500. The image of the gel was analyzed with Image Quant 5.2 software. The pH- and hydrophobicity-dependent DNA dissociation was also quantified by investigating absorbance of the filtrates at 260 nm. The concentration of DNA filtrates was quantified using the absorbance of a solution of 1.275 μM $d(GT)_{20}$ as standard that represents the total DNA content of PDN (calculated from PDN concentration with ratiometric quantification).

Endocytosis-mediated cellular uptake of PDN was evaluated by co-localization with FITC-labeled dextran. Human bladder cancer cells (ATCC 5637) were cultured in sterile chamber slides and treated with complete media containing PDN (2 μg/mL) and FITC-labeled dextran (1 mg/mL), then incubated overnight at 37 °C, and, next morning, washed with sterile PBS and imaged using a Zeiss Axiovert LSM-510 microscope. PDN were excited using the 633 nm laser and emission was collected with the 650 nm long-pass filter set. FITC-labeled dextran was excited using the 488 nm argon laser and emission collected with 505-530 nm bandpass filter set. DIC images of cells were collected in a separate channel for overlay. The co-localization analysis was done using LSM 510 software (Carl Zeiss).

Tissue culture cytotoxicity and apoptosis assays

Human bladder cancer cells (ATCC 5637) were cultured in complete media (RPMI + 10% FBS). The cells were then treated with complete media containing nanoparticle at final concentrations of 0, 1, 2, 5 μg/mL followed by incubation overnight then washed with PBS. One of two plates was then exposed to 420 nm blue light (Trophy Skin Blue MD) at a power density of 2.3 μW/cm^2 for 10 min followed by incubation for 24 h. Cell viability was assessed using the CellTiter 96 Proliferation Assay reagent (Promega) following the manufacturer's instructions. Apoptosis was assessed using the Caspase Glo 3/7 assay (Promega) with similar procedures except PDN concentration was evaluated at 0 or 2 μg/mL. Luminescence was measured using GENios (TECAN) microplate reader. Each set of data (net absorbance) was expressed as a percentage, considering the no treatment group as 100%.

Light-dependent membrane damage by PDN

Localized membrane damage of PDN upon blue light irradiation was evaluated using confocal microscopy to detect calcein-AM retention, a cytoplasm-localizing fluorescent dye. Cells were cultured in each of two sterile chamber slides and treated with complete media containing PDN (0 or 2 μg/mL), incubated overnight at 37 °C, washed with PBS followed by addition of Calcein-AM (Invitrogen) at final concentration 2.5 μM, and incubated for 15 min at 37 °C. One of the two chamber slides was then exposed to 420 nm blue light for 10 min. Confocal microscopy was performed as mentioned in the FITC-dextran experiment.

Light-dependent ROS generation and membrane lipid peroxidation by PDN

PDN suspension was prepared in 20 mM phosphate buffer (pH 7.4) as described above to a final concentration of 250 μg/mL. Acetonitrile buffer mixture was prepared by adding appropriate amount of 100 mM sodium phosphate and acetonitrile with water. PDN suspension was added to the mixture (5 μg/mL) followed by addition of the dye C11 Bodipy to final concentration 20 μM in a 96 well black flat bottom plate (Costar). Mixtures were prepared in triplicates in two plates. One of the plates was then exposed to the blue light for 2 min immediately followed by scanning with Tecan-Safire-II microplate reader in fluorescence detection mode with 480 nm excitation and 500-800 nm emission. Slit opening was set to 10 nm, and reading was average for 5 actuations.

Membrane lipid peroxidation upon blue light irradiation of cancer cells treated with PDN was evaluated using confocal microscopy detecting a membrane localizable fluorescent dye (C11-Bodipy). Microscopy was performed as described for confocal microscopy experiments including an additional channel for detecting non-oxidized dye, excited with a 543 nm He-Ne laser and emission was collected using 565-615 bandpass filter.

Detection of light-dependent membrane damage by PDN

PDN-mediated membrane damage upon blue light irradiation was detected by Transmission Election Microscopy (TEM). Cell culture and PDN treatment, including blue light irradiation, were performed in 6-well clear bottom plates (Costar) following the same procedure as for the *in vitro* cytotoxicity assay with the PDN concentration 0 or 2 μg/mL. Cells were fixed with 2.5% glutaraldehyde and treated with 2% osmium tetroxide, then dehydrated gradually followed by embedding in the resin and sectioning for TEM investigation.

Antitumor activity of PDN

All animal experiments were performed in accordance with protocols approved by the Wake Forest School of Medicine Animal Care and Use Committee. Six week old female nude mice were ordered from NCI. Tumor xenografts were generated by subcutaneous injection of 1.5×10^6 human bladder cancer cells suspended in 200 μL of 1:1 PBS/Matrigel (BD bioscience) in both flanks of 10 female nude mice. Mice were used for experimental procedures 3 weeks following inoculation with tumor cells, after tumor size had reached approximately 75 mm^3. Each of 10 mice was injected with 100 μL of 250 μg/mL PDN suspension in one flank and 100 μL saline in the other flank. Approximately 12 h later, tumors on both flanks of 6 mice were irradiated with a blue beam of 420 nm for 3 min. The source laser for these studies was a Mira 900 (Coherent Inc., Santa Clara, CA), a mode-locked femtosecond Ti:Sapphire laser. The pulses were approximately 90 femtoseconds at a wavelength of 840 nm with an average power of 600 mW. The beam was transmitted directly into the tumor using a multimode optical fiber (SFS105/125Y, Thorlabs Inc., Newton, NJ). The output power at the final end of the fiber was 100 mW. The remaining four mice were treated identically but were not exposed to the laser. The laser irradiation was performed every 5th day for a total of five doses. Tumor sizes were measured using calipers and tumor volumes were calculated using the formula $xy^2 \pi/6$ (where x and y are the long and short diameters of the tumor, respectively). The tumors were analyzed as four independent groups: i) no treatment; ii) light-only; iii) PDN-only; iv) PDN + light. Relative tumor volumes (V/V_o) were graphed vs. time (where V is the present tumor volume and V_o was the tumor volume when treatment started). Repeated measures mixed models were fit to compare tumor volumes between groups. In these models, animals were treated as random effects and group (four-levels) and time (days) were treated as fixed-effects. The group-by-time interaction was examined to determine whether the rate of change in tumor volume differed over time among the four groups. All statistical analyses were performed using SAS 9.1.

Histopathological analysis of tumor tissue

At the conclusion of the study animals were sacrificed and tumors were excised and placed in 4% paraformaldehyde solution overnight at ambient temperature. The following day, tumors were embedded in molten paraffin and thin sections were prepared from different layers of tumors and placed on glass slides followed by H&E staining.

Results

Biophysical properties of porphyrin:DNA nanoparticles

Meso-tetra-4-pyridyl porphine (MTP – Figure 1, *A*) is soluble in aqueous solution only at acidic pH (<5.5) and forms

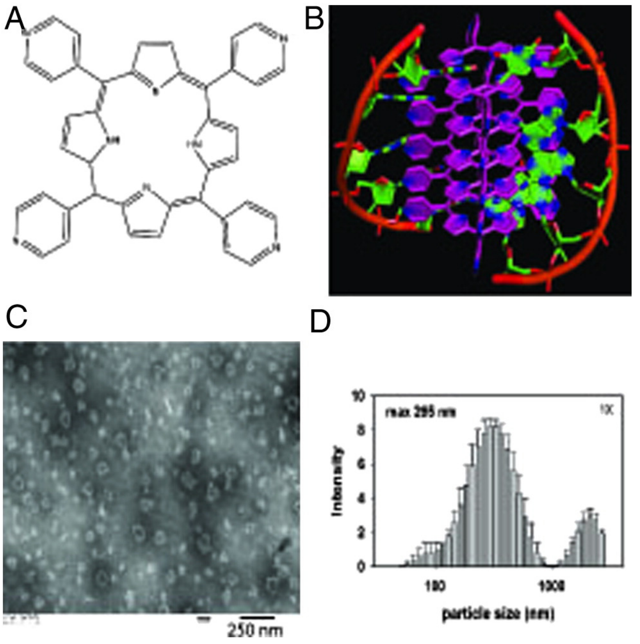

Figure 1. Discrete porphyrin:DNA nanoparticles (PDN) form upon sonication of MTP porphyrin with ssDNA. **(A)** Structure of the MTP porphyrin used for these studies. **(B)** Molecular model of PDN nanocomplex showing both porphyrin-porphyrin and porphyrin:DNA interactions. **(C)** TEM image of PDN nanoparticles. **(D)** DLS analysis of PDN hydrodynamic radius distribution.

aggregates in solution near physiological pH. Sonication of MTP in the presence of single-stranded DNA at pH 7.4, however, permitted recovery of discrete, nano-sized particles composed of both porphyrin and DNA (porphyrin:DNA nanoparticles – PDN; Figure 1, *B*). Production of nanoparticles (Figure S1, Supporting Information) was DNA-dependent and the ratio of porphyrin to DNA (d(GT)$_{20}$) was determined to be ~19:1 (mol/mol) or about two DNA nucleobases per MTP based upon the UV absorbances calculated from the acid-dissolved nanoparticles (Table S1 and Figure S2, Supporting Information). The size and shape of the PDN were investigated using transmission electron microscopy (TEM – Figure 1, *C*) and the hydrodynamic properties of PDN were investigated using dynamic light scattering (DLS – Figure 1, *D*). TEM images revealed irregular shaped particles with average length and diameter ~60 nm (Figure S3, Supporting Information) while DLS revealed PDN in aqueous solution had an average hydrodynamic radius of ~295 nm (Figure 1, *D*).

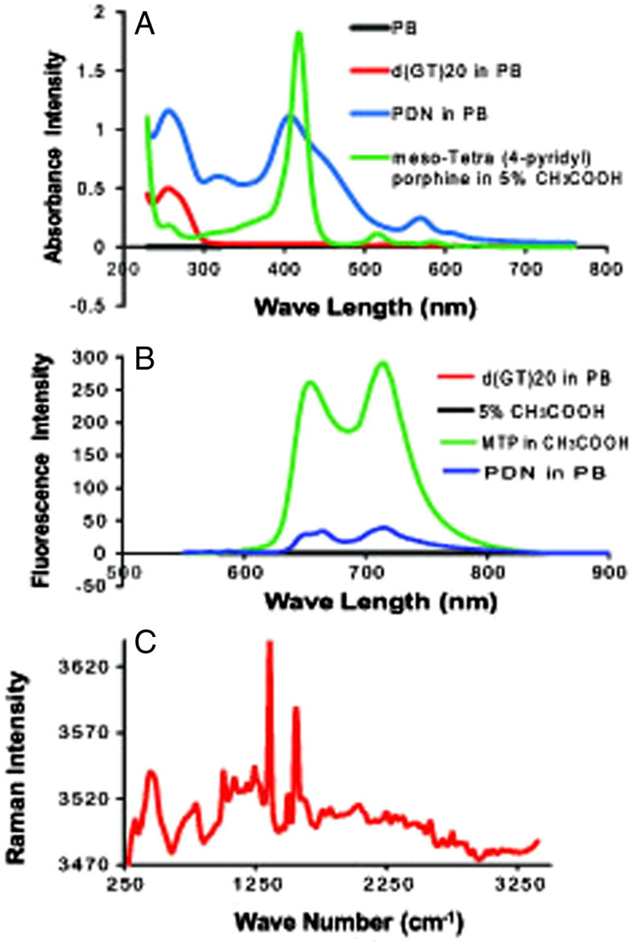

Figure 2. Spectroscopic characterization of PDN reveals the physical properties of the porphyrin are altered in the PDN complex. **(A)** Absorbance spectra for PDN (blue), MTP monomer (green), DNA (red), and phosphate buffer (black). **(B)** Fluorescence spectra for MTP monomer (green), PDN (blue), DNA (black), and 5% acetic acid (magenta). **(C)** Raman spectrum for PDN.

PDN were characterized by UV-Vis, fluorescence, and Raman spectroscopies to determine to what extent the context of the PDN complex altered the electronic properties of the constituent porphyrin and DNA. UV-Vis spectra for PDN revealed the absorbance at 260 nm from the DNA was little changed relative to free DNA while the Soret (S0->S2) band[22] was slightly red-shifted and broadened for PDN relative to MTP (Figure 2, *A*). The Q band (S0->S1)[23] at 535 nm was also enhanced and sharpened for the PDN relative to the free porphyrin. Fluorescence spectra for PDN with excitation at 420 nm showed that the emission maxima at 660 and 725 nm for the MTP monomer were substantially quenched for PDN with emission maxima reduced ~25-fold (Figure 2, *B*). Raman spectra (457.9 absorption; Figure 2, *C*) revealed two sharp peaks at 1360 and 1555 cm^{-1} for PDN similar to resonances assigned previously to ($\nu_{(X\beta-X\beta)}+(X\beta-H)$) and ($\nu_{(X\alpha-N)}+\delta_{(X\beta-H)}$) for tetrasulfonated tetraphenyl porphyrin (TSSP) upon electrode binding,[24] consistent with surface-enhancement of Raman spectra for MTP in the context of PDN. Together, the spectroscopic properties reveal an altered electronic structure for MTP in the context of PDN that is consistent with $\pi-\pi$ stacking of porphyrins with DNA nucleobases contributing significantly to PDN assembly.

Hydrophobicity-dependent DNA release and endosomal uptake of PDN

The stability of PDN as a function of pH and solvent hydrophobicity was investigated to gain insight into the nature of forces promoting complex stability. PDN stability at physiologically-relevant pH is mainly dependent on hydrophobic interactions (Figure 3, *A* and *B* and S4, S5, Supporting Information). Acidification of PDN to pH 5.1 may also enhance its dissociation process, as indicated by small amount of DNA release, due to pyridyl nitrogen protonation. Approximately 70% of total DNA

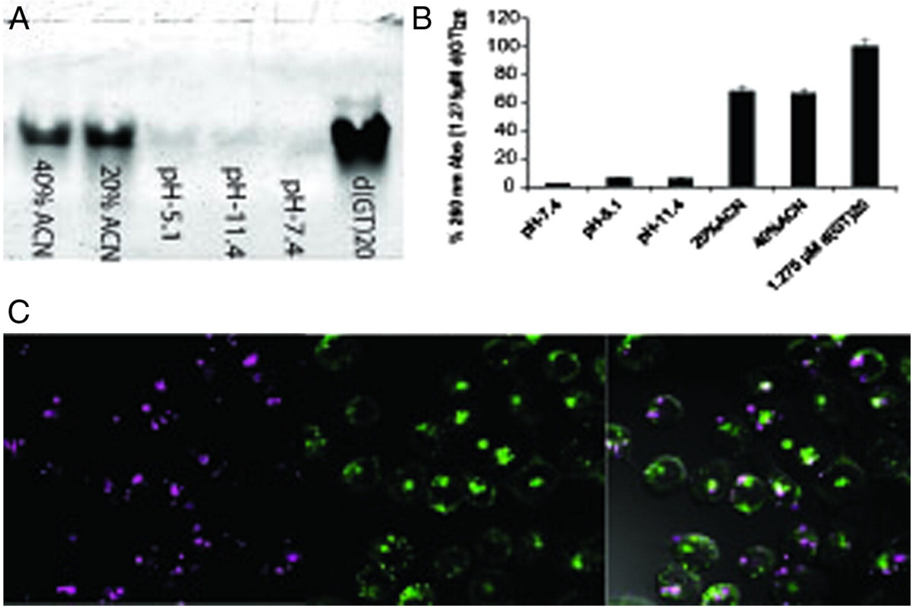

Figure 3. PDN-disassembly as a function of pH and solvent hydrophobicity. **(A)** 15% native polyacrylamide gel electrophoresis of DNA filtrates released upon incubation at pH 7.4, 11.4, 5.1 and at 20%, 40% acetonitrile containing mixture. A solution of 2.5 μM $d(GT)_{20}$ was included as standard. **(B)** Representative graphs of 260 nm UV absorbance of DNA filtrates as mentioned above. A solution of 1.275 μM $d(GT)_{20}$ was included as representative of total DNA content of the PDN suspension calculated from ratiometric quantification. **(C)** Confocal microscopy images evaluating endosomal uptake of PDN. Cells were co-treated with PDN (magenta; left) and FITC labeled dextran (green; middle). Endosomal PDN uptake was demonstrated by colocalization both fluorescence in overlay with DIC image of the cell (right).

was released upon PDN dissociation in 20% and 40% acetonitrile solution; while pH 5.1 and 11.4 induced ~7% of total DNA release in the 100% aqueous environment (Figure 3, *A* and *B*) and no DNA release was observed in pH 7.4 at 100% aqueous environment. However *in vitro* acidification of PDN to pH 3.0 or below leads to complete PDN dissociation immediately due to full protonation of the porphyrin molecules including central pyrrol rings.[25,26] While the hydrophobicity-dependence of PDN dissociation is consistent with disruption of hydrophobic base stacking between DNA and MTP, the DNA release from PDN was favored by increasing hydrophobicity of the solvent system by acetonitrile addition (Figure 3, *A* and *B* and S4, Supporting Information). Thus, the data are consistent with $\pi - \pi$ stacking between DNA nucleobases and pyridyl side chains of MTP significantly contributing to PDN stability. The hydrophobicity-dependence of PDN dissociation *in vitro* caused us to investigate to what extent PDN dissociate in hydrophobic environments *in vivo*. Significantly, hydrophobic environment of plasma membrane potentially promotes PDN disassembly by dynamic hydrophobic interactions (Figure S5, Supporting Information).[27,28]

Endosomal uptake of PDN was demonstrated by co-localization of PDN with endosome-localizing FITC-dextran complex.[29–31] Co-localization data showed approximately 45% of the PDN gets internalized by endocytosis (overlap coefficient ~0.7)[32,33] (Figure 3, *C*). While about half of the PDN undergoes endocytosis, a significant fraction remains associated with the cell membrane as demonstrated by the co-localization of PDN with membrane localizing dye Bodipy in a circular peripheral pattern (Figure S6, supporting Information). Endosomes are acidic in nature and may promote PDN dissociation upon cellular internalization in addition to interactions with the hydrophobic lipid membrane. Increased acidity, associated with the tumor microenvironment raises the possibility that PDN may dissociate in tumor tissue. We performed confocal microscopy experiments with fluorescently-(6-FAM-) labeled DNA and evaluated DNA release upon PDN dissociation (Figure S5, Supporting Information). Confocal microscopy analysis demonstrated DNA dissociation with a co-localization coefficient 0.083 indicating less than 10% of total DNA co-localizes with porphyrin.

Light-dependent cytotoxicity of PDN

The cytotoxicity of PDN towards human bladder cancer cells was evaluated to determine to what extent these nano-sized complexes are cytotoxic towards malignant cells in a light-dependent manner (Figure 4 and Figures S8-S10, Supporting Information). ROS resulting from PDN dissociation upon interacting with the plasma membrane could, upon light stimulation, result in lipid peroxidation producing subsequent loss of membrane integrity and cell death (Figure 4, *A*). Cell viability assays demonstrated PDN are cytotoxic to bladder cancer cells in a light-dependent manner (Figure 4, *B*). Interestingly, the light-dependent cytotoxicity of PDN towards bladder cancer cells is relatively independent of PDN concentration consistent with a threshold level of membrane damage inducing cell death. The light-dependent cytotoxicity of PDN was accompanied by only a slight increase in apoptosis (Figure 4, *C*), with little DNA damage (Figure S14, Supporting Information) and no effect of z-VAD rescue consistent with cell death being predominantly non-apoptotic.

To gain further insight into the nature of cell death, bladder cancer cells were pre-treated with the cytoplasm-localizing dye

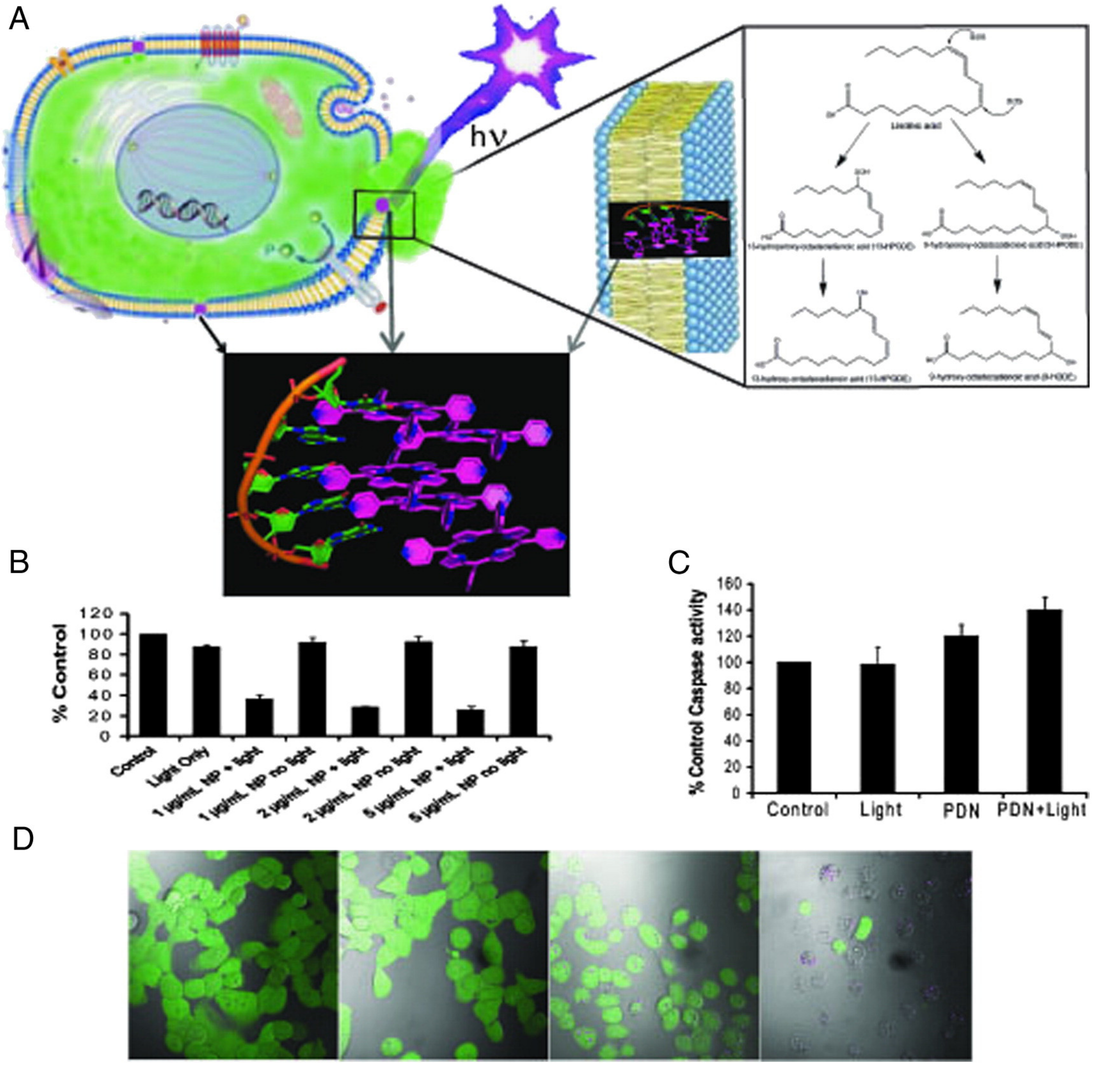

Figure 4. PDN are cytotoxic to bladder cancer cells via localized damage to the plasma membrane as a consequence of light-activated oxidation of membrane lipids. **(A)** Depiction of a cancer cell with PDN localized to the plasma membrane and with light (hν) irradiation; inset displays an enlargement of the lipid bilayer of the plasma membrane with a PDN complex internalized in the membrane and shows further structures for the 9-HODE and 13-HODE lipid peroxidation products detected by mass spectrometry following PDN/light treatment. The green efflux reflects loss of calcein-AM dye resulting from membrane damage. **(B)** Cytotoxicity assay results showing PDN/light reduces bladder cancer viability. **(C)** Apoptosis assay results showing PDN-mediated cell death is predominantly non-apoptotic. **(D)** Confocal microscopy images displaying overlay of calcein-AM (green) fluorescence on DIC images for bladder cancer cells following treatment with (left – right) no-treatment, light-only, PDN-only, PDN/light. Treatment with PDN/light resulted in efflux of calcein-AM.

calcein-AM and the effects of PDN and light on calcein retention were investigated. Treatment with PDN and light resulted in dye efflux for nearly all cells (Figure 4, *D*) while treatment with PDN-only or light-only did not stimulate dye efflux (Figure 4, *D*). The results indicate cell death is accompanied by a loss of membrane integrity. Interestingly, the free radical scavenger N-acetyl cysteine (NAC) could not rescue cells from the light-mediated cytotoxicity of PDN (Figure S10, Supporting Information). The results are consistent with PDN exerting localized cell damage that is not affected by the REDOX state of the cell.

In vitro heating and ROS production of PDN

Porphyrins are widely used for PDT[34] in which absorbed light is used for production of cytotoxic ROS. The UV-Vis spectra for PDN indicated UV/Vis absorption was attenuated by ~2 fold relative to the same concentration of free MTP (Figure 2, *A*) while fluorescence for the PDN complex is quenched by ~25 fold (Figure 2, *B*) consistent with absorbed light being dissipated as heat and/or used for ROS production. The time- and concentration-dependence for heating of aqueous solutions of PDN was evaluated to determine whether temperature increases of a magnitude required for cell-killing could be induced (Figure S7, Supporting Information). PDN are not efficient transducers of heat although measurable temperature increases were detected upon photo-stimulation.

Cell death is mediated by oxidation of membrane lipids causing localized damage

The light-dependent cytotoxic mechanism of PDN was further investigated using confocal microscopy, TEM, and mass

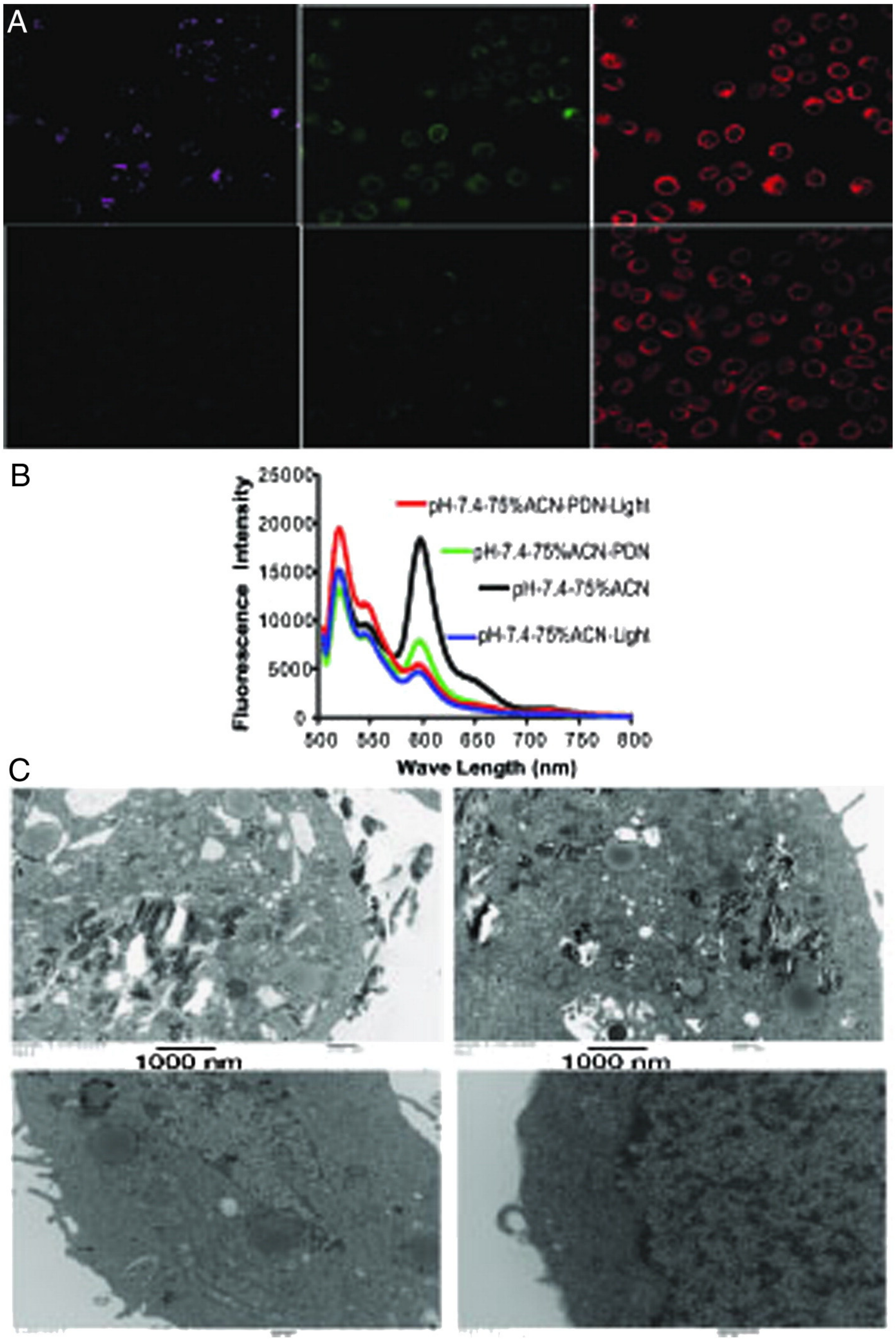

Figure 5. PDN/Light treatment results in oxidation of plasma membrane lipids and localized membrane damage. **(A)** Confocal microscopy images displaying free porphyrin (left – magenta), oxidized membrane lipids detected with Bodipy (center – green), and non-oxidized membrane lipids detected with Bodipy (right-red). The top panels are from bladder cancer cells treated with PDN/light while the bottom panels are from light-only cells. **(B)** Representative fluorescence spectrum of dye c11 bodipy in presence of PDN + light (red); PDN (green); light only (blue) and control (black) with excitation 480 nm in pH 7.4 in 75% ACN + 25% aqueous solution mixture. **(C)** TEM images of bladder cancer cells treated with PDN/light (top-left), PDN-only (top-right), light-only (bottom-left), and no-treatment (bottom-right).

spectrometry to determine if physical damage to the plasma membrane and endosomal compartments were important for PDN-mediated cell death (Figure 5 and Figure S11-13, Supporting Information). The nature of the observed membrane damage was investigated using the fluorescent membrane-localizing dye Bodipy[35,36] to visualize the occurrence of oxidized lipids in the plasma membrane of bladder cancer cells treated with PDN and light (Figure 5, *A*). The dye undergoes a change in absorbance from red to green upon oxidation. The results demonstrate that treatment of bladder cancer cells with PDN and light, but not light-only, resulted in increased levels of oxidized lipids as indicated by the elevated level of green

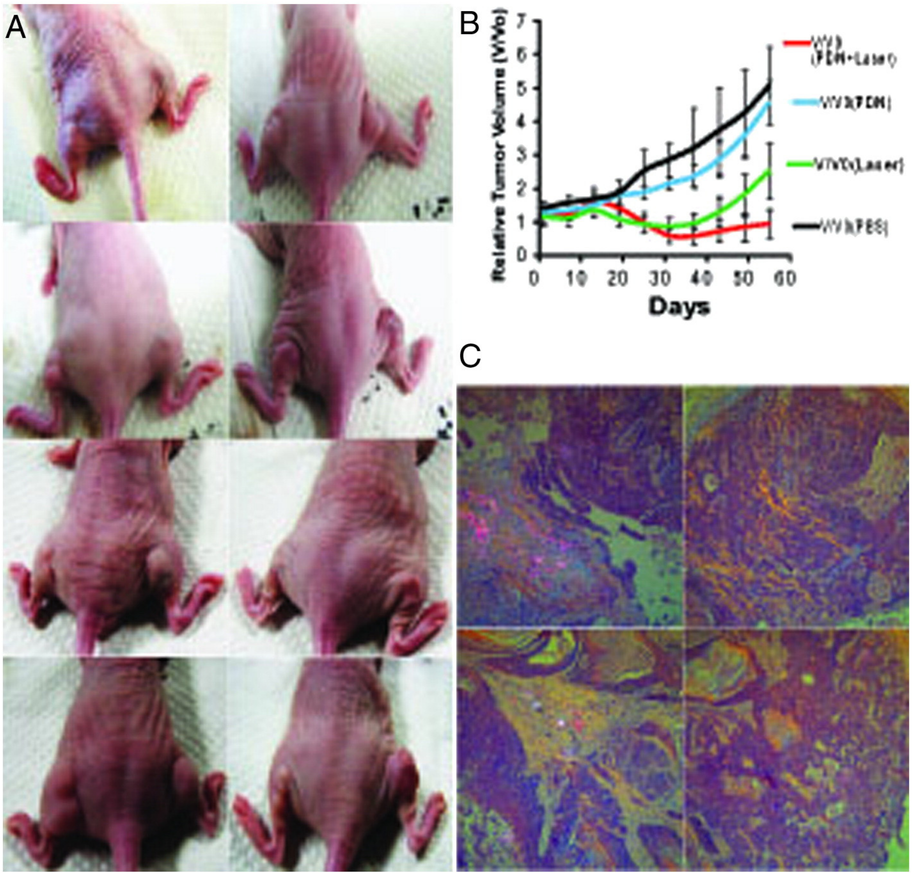

Figure 6. PDN/light treatment displays significant anti-tumor activity *in vivo*. **(A)** Representative tumors from the four treatment groups at day 0 (top row – prior to any treatment), day 1 (2nd row – after initial treatments), day 25 (3rd row – at the conclusion of light treatment), and day 55 (bottom row – end of study). The left mouse, left flank (L, L) received no treatment; the left mouse, right flank (L-R) received PDN-only. The right mouse, left flank (R, L) received PDN/light and the right mouse, right flank (R, R) received light-only. **(B)** Plot of relative volumes for bladder cancer xenografts over time following treatment with PDN/light (red), light-only (green), PDN-only (blue), no treatment (black). **(C)** Histopathological analysis of tumor tissue. Polarization detection as part of histological analysis for PDN in tissues excised from animals at the conclusion of the study receiving the following treatments: (top-left) – PDN/light; (top-right) – light-only; (bottom-left) – PDN-only; (bottom-right) – no treatment.

fluorescence (Figure 5, *A*). The ROS production by PDN upon light stimulation was further confirmed *in vitro*. Experimental results evidenced for PDN mediated C11-Bodipy oxidation occurred selectively in a light-dependent manner in solvent sys1tems that favored PDN dissociation such as the presence of acetonitrile (Figure 5, *B*). TEM images revealed PDN were associated with the plasma membrane and internalized, likely in endosomes, and that substantial membrane damage and vacuole formation was observed proximal to nanoparticles in a light-dependent manner (Figure 5, *C* and S11, Supporting Information). Localized membrane damage, caused by PDN/light mediated oxidation, leads to necrotic cell death.[37,38] The presence of oxidized lipids in the plasma membrane was investigated further using mass spectrometry. Mass spectrometry confirmed that elevated levels of 9-HODE and 13-HODE, products resulting from lipid peroxidation,[39] occurred selectively in cells treated with PDN and light (Figure S12, S13). Together, these results indicate cell death following treatment with PDN and light occurred from localized membrane damage leading to a loss of plasma membrane integrity.

PDN display light-dependent antitumor activity in vivo

The light-dependent cytotoxicity of PDN towards bladder cancer cells in tissue culture invites the question of whether PDN can be used for light-dependent reduction or eradication of tumors *in vivo*. To address this question, we formed xenograft tumors bilaterally on the flanks of nude mice (Figure 6, *A* and Figure S15, Supporting Information). Initial tumor volumes were ~75 mm^3 and there was no difference among the treatment groups at baseline. Tumors were treated by direct injection of either PDN or a saline solution. The tumor groups were further divided into light-treated and mock-treated groups to create four groups: i) no treatment; ii) light-only; iii) PDN-only; iv) PDN + light. Light treatment was achieved by inserting a fiber-optic cable into the tumor followed by treatment with 420 nm laser light for 3 min. Tumors that were not light-treated underwent a similar number of identical procedures introducing the fiber-optic cable without light exposure. The time-dependence of tumor growth and regression is shown in Figure 6, *B*. Beginning around day 20 tumors treated with either light or

PDN + light displayed tumor regression while the untreated tumors began to display more rapid growth. Tumors treated with PDN and light displayed significant tumor regression that was superior to no treatment or treatment with PDN-only beginning on day 20 and achieving statistical significance at day 30 and persisting until the conclusion of the study ($P < 0.05$). Tumor regression following treatment with PDN and light was significantly greater than for light-only beginning on day 40 and achieving statistical significance at day 49 and persisting until completion of the study ($P < 0.05$). The results demonstrate that PDN display light-dependent anti-tumor activity *in vivo*.

Histopathological analysis of tumor tissue following treatment with PDN

At the conclusion of the *in vivo* study, tumor tissue was removed from sacrificed mice and sectioned for morphologic evaluation. In all study groups, sections showed subcutaneous tumoral deposits comprised of urothelial carcinoma with high-grade cytology and partial keratinization. Tumor tissue from mice in the control group that received neither nanoparticle nor light showed only subcutaneous tumoral deposits. Polarization revealed no polarizable nanoparticles (Figure 6, *C* and Figure S16, Supporting Information) and there was minimal fibrosis, chronic inflammation, or reparative changes. Tumor tissue from mice treated with light-only revealed similar features as those mice in the control group. For mice in both the PDN-only and the PDN/light groups, polarization revealed the presence of nanoparticles confirming the persistence of PDN at the site of injection for several weeks allowing multiple exposures from single administered dose (Figure 6, *C* and Figure S16, Supporting Information). For the PDN-only group, tumor was absent in areas where nanoparticle was present demonstrating PDN having a native mild tumor abortive effect even in the absence of light. For the PDN/light group, tumor was also absent in the areas where nanoparticle was present with marked fibrosis, chronic inflammation, and reparative changes. This supports a potent tumor abortive effect likely enhanced by light excitation; a result which already accentuates the native anti-tumor activity of PDN. Some areas of tumor not displaying polarizable nanoparticles, however, showed tumor re-growth consistent with incomplete penetration of nanoparticles. Another advantage appears that the range of killing activity is confined to zones around PDN deposition, allowing for precise margins with this therapeutic approach.

Discussion

The present studies demonstrate that discrete nano-sized particles can be obtained from non-covalent assembly of MTP and DNA under controlled conditions. Discrete nanoparticles do not form from MTP in the absence of DNA indicating DNA: porphyrin interactions are critical for PDN assembly. The ratio of porphyrin to DNA in PDN (~19:1) (mol/mol) is consistent with two nucleobases from each DNA 40-mer interacting with each porphyrin. Thus, approximately half the pyridyl side chains in each MTP (Figure 1, *A*) may be engaged in interactions with DNA nucleobases (Figure 1, *B*). The spectroscopic results are consistent with $\pi - \pi$ stacking between pyridyl side chains and DNA nucleobases as being a principal driving force for nanoparticle assembly.[40,41] PDN display quenching of porphyrin fluorescence and increased intensity and sharpness for Raman spectra similar to that observed upon surface-enhancement for free porphyrins. Dissociation of PDN was favored in the hydrophobic solvent system, consistent with PDN stability result from $\pi - \pi$ stacking between PDN and DNA with aqueous solubility conferred by the phosphodiester backbone of DNA.[42,43] The nature of PDN disassembly in the hydrophobic environment, releasing the DNA component, could be significant for DNA-based therapeutics delivery upon PDN dissociation in the hydrophobic milieu of cell membrane.

We have demonstrated that PDN cause cell death predominantly via localized membrane damage resulting in necrosis. While conventional photosensitizers can induce membrane damage upon light stimulation, a variety of other cellular organelles, including the mitochondria,[44] are also potential sites for PDT-induced damage. Our studies demonstrate PDN localize to the plasma membrane (Figure S6, Supporting Information) and also undergo internalization via endocytosis (Figure 3, *C*). Upon interaction with cellular components the fluorescence of FAM-labeled DNA dissociates from porphyrin fluorescence (Figure S5, Supporting Information) consistent with PDN disassembly in the hydrophobic environment of cell membranes or vesicles. Photo-mediated damage by porphyrin results in loss of plasma membrane integrity and vacuole formation (Figure 4, *D* and *C* and S11, Supporting Information). The plasma membrane damage is caused by lipid oxidation (Figure 5, *A* and *C* and S11, Supporting Information) and specifically generation of the oxidized fatty acids 9-HODE and 13-HODE (Figure S12, S13, Supporting Information).

Importantly, PDN/light treatment of bladder cancer xenografts resulted in significant reduction in tumor volumes *in vivo* (Figure 6, *A* and *B*). Histopathological analysis of tumor tissue revealed, PDN/light displayed strong tumorpathic properties and elicited inflammatory and reparative changes associated with an immune response (Figure 6, *C* and S16, Supporting Information). No tumor tissue was identified in regions where PDN were localized indicating PDN/light treatment exerts powerful anti-tumor effects with very tight margins. Although mild anti-tumor activity was observed in case of PDN-only treatment probably due to basal level ROS production and immune response,[45,46] this mild anti-tumor effect is not likely to be sufficient for the treatment of aggressively growing tumors in advanced cases.[47,48] These results indicate PDN/light may be highly effective for cancer treatment in humans. Localized retention of the PDN provides the opportunity for multiple light exposures as required to eliminate remaining or re-growing malignant tissue. However, the concern of uniform delivery of PDN needs to be addressed to achieve a significant overall anti-tumor effect.

The present studies demonstrate the potential application of PDN for treatment of solid tumors via intra-tumoral injection.[49–51] However, in future studies, cancer cell specific DNA or RNA aptamers[52,53] could be conjugated to the PDN for molecular targeting upon systemic injection. PDN could be developed as multi-modality nanoparticles[54] by replacing the presently used $d(GT)_{20}$ with cytotoxic DNA like FdUMP[10][55] thus DNA-release may contribute to the overall therapeutic response.

Presently performed experiments indicated PDN readily dissociate upon cellular internalization as a consequence of the hydrophobic environment in the cell membrane releasing DNA payload. However detailed, time-dependent DNA dissociation kinetics should be examined in future studies. Dissociated therapeutic nucleic acid, if used, may exert additional anti-tumor activity providing a therapeutic advantage not realizable using conventional photosensitizers or nanoparticles that do not include a DNA component. Importantly, PDN are biocompatible and elicited no apparent morbidity upon *in vivo* administration.[56,57]

Acknowledgment

The authors acknowledge Dr. Baidyanath Saha for helping with TEM image analysis; Chris Stuart for helping with *in vivo* experiments; Michael Samuel for helping with mass-spectrometry experiment; Dr. David A. Horita for helping with nanoparticle model building; and WFU Department of Physics for use of laser facilities.

Appendix A. Supplementary data

Supplementary data to this article can be found online at http://dx.doi.org/10.1016/j.nano.2013.07.019.

References

1. Gong X, Milic T, Xu C, Batteas JD, Drain CM. Preparation and characterization of porphyrin nanoparticles. *J Am Chem Soc* 2002;**124**:14290-1.
2. Liang XL, Li XD, Yue XL, Dai ZF. Conjugation of porphyrin to nanohybrid cerasomes for photodynamic diagnosis and therapy of cancer. *Angew Chem Int Edit* 2011;**50**:11622-7.
3. Wang ZC, Medforth CJ, Shelnutt JA. Porphyrin nanotubes by ionic self-assembly. *J Am Chem Soc* 2004;**126**:15954-5.
4. Drain CM, Smeureanu G, Patel S, Gong XC, Garno J, Arijeloye J. Porphyrin nanoparticles as supramolecular systems. *New J Chem* 2006;**30**:1834-43.
5. De Napoli M, Nardis S, Paolesse R, Vicente MG, Lauceri R, Purrello R. Hierarchical porphyrin self-assembly in aqueous solution. *J Am Chem Soc* 2004;**126**:5934-5.
6. Lauceri R, De Napoli M, Mammana A, Nardis S, Romeo A, Purrello R. Hierarchical self-assembly of water-soluble porphyrins. *Synthetic Met* 2004;**147**:49-55.
7. Bellacchio E, Lauceri R, Gurrieri S, Scolaro LM, Romeo A, Purrello R. Template-imprinted chiral porphyrin aggregates. *J Am Chem Soc* 1998;**120**:12353-4.
8. Anand S, Ortel BJ, Pereira SP, Hasan T, Maytin EV. Biomodulatory approaches to photodynamic therapy for solid tumors. *Cancer Lett* 2012;**326**:8-16.
9. Davila ML. Photodynamic therapy. *Gastrointest Endosc Clin N Am* 2011;**21**:67-79.
10. Ethirajan M, Chen Y, Joshi P, Pandey RK. The role of porphyrin chemistry in tumor imaging and photodynamic therapy. *Chem Soc Rev* 2011;**40**:340-62.
11. Josefsen LB, Boyle RW. Unique diagnostic and therapeutic roles of porphyrins and phthalocyanines in photodynamic therapy, imaging and theranostics. *Theranostics* 2012;**2**:916-66.
12. O'Connor AE, Gallagher WM, Byrne AT. Porphyrin and nonporphyrin photosensitizers in oncology: preclinical and clinical advances in photodynamic therapy. *Photochem Photobiol* 2009;**85**:1053-74.
13. Walton SP, Wu M, Gredell JA, Chan C. Designing highly active siRNAs for therapeutic applications. *FEBS J* 2010;**277**:4806-13.
14. Ananyan G, Avetisyan A, Aloyan L, Dalyan Y. The stability of DNA-porphyrin complexes in the presence of Mn(II) ions. *Biophys Chem* 2011;**156**:96-101.
15. Bennett M, Krah A, Wien F, Garman E, Mckenna R, Sanderson M, et al. A DNA-porphyrin minor-groove complex at atomic resolution: The structural consequences of porphyrin ruffling. *P Natl Acad Sci USA* 2000;**97**:9476-81.
16. D'Urso A, Mammana A, Balaz M, Holmes AE, Berova N, Lauceri R, et al. Interactions of a tetraanionic porphyrin with DNA: from a Z-DNA sensor to a versatile supramolecular device. *J Am Chem Soc* 2009;**131**:2046-7.
17. Geacintov NE, Ibanez V, Rougee M, Bensasson RV. Orientation and linear dichroism characteristics of porphyrin DNA complexes. *Biochemistry* 1987;**26**:3087-92.
18. Lipscomb LA, Zhou FX, Presnell SR, Woo RJ, Peek ME, Plaskon RR, et al. Structure of a DNA—Porphyrin complex. *Biochemistry* 1996;**35**:2818-23.
19. Jain RK, Stylianopoulos T. Delivering nanomedicine to solid tumors. *Nat Rev Clin Oncol* 2012;**7**:653-64.
20. Maeda H. Macromolecular therapeutics in cancer treatment: The EPR effect and beyond. *J Control Release* 2012;**164**:138-44.
21. Plaetzer K, Krammer B, Berlanda J, Berr F, Kiesslich T. Photophysics and photochemistry of photodynamic therapy: fundamental aspects. *Lasers Med Sci* 2009;**24**:259-68.
22. Nemykin VN, Hadt RG. Interpretation of the UV-Vis spectra of the meso(ferrocenyl)-containing porphyrins using a TDDFT approach: is Gouterman's classic four-orbital model still in play? *J Phys Chem A* 2012;**114**:12062-6.
23. Lan M ZH, Yuan H, Jiang C, Zuo S, Jiang Y. Absorption and EPR spectra of some porphyrins and metalloporphyrins. *Dyes Pigments* 2007;**74**:357-62.
24. Cotton T, Schultz SG, van Duyne RP. Surface-enhanced resonance Raman scattering from water-soluble adsorbed on a silver electrode. *J Am Chem Soc* 1982;**104**:6528-32.
25. Cunderlikova B, Kaalhus O, Cunderlik R, Mateasik A, Moan J, Kongshaug M. pH-dependent modification of lipophilicity of porphyrin-type photosensitizers. *Photochem Photobiol* 2004;**79**:242-7.
26. Stepanek P, Andrushchenko V, Ruud K, Bour P. Porphyrin protonation studied by magnetic circular dichroism. *J Phys Chem A* 2012;**116**:778-83.
27. Chandler D. Interfaces and the driving force of hydrophobic assembly. *Nature* 2005;**437**:640-7.
28. McMahon HT, Gallop JL. Membrane curvature and mechanisms of dynamic cell membrane remodelling. *Nature* 2005;**438**:590-6.
29. Bayer N, Schober D, Prchla E, Murphy RF, Blaas D, Fuchs R. Effect of bafilomycin A1 and nocodazole on endocytic transport in HeLa cells: implications for viral uncoating and infection. *J Virol* 1998;**72**:9645-55.
30. Lencer WI, Weyer P, Verkman AS, Ausiello DA, Brown D. FITC-dextran as a probe for endosome function and localization in kidney. *Am J Physiol* 1990;**258**:C309-17.
31. Shurety W, Stewart NL, Stow JL. Fluid-phase markers in the basolateral endocytic pathway accumulate in response to the actin assembly-promoting drug Jasplakinolide. *Mol Biol Cell* 1998;**9**:957-75.
32. Manders FJVEMM, Aten JA. Measurement of co-localization of objects in dual-colour confocal images. *J Microsc* 1993;**169**:375-82.
33. Zinchuk V, Zinchuk O, Okada T. Quantitative colocalization analysis of multicolor confocal immunofluorescence microscopy images: pushing pixels to explore biological phenomena. *Acta Histochem Cytochem* 2007;**40**:101-11.
34. Allison RR, Sibata CH. Oncologic photodynamic therapy photosensitizers: a clinical review. *Photodiagnosis Photodyn Ther* 2010;**7**:61-75.
35. Drummen GP, van Liebergen LC, Op den Kamp JA, Post JA. C11-BODIPY(581/591), an oxidation-sensitive fluorescent lipid peroxidation probe: (micro)spectroscopic characterization and validation of methodology. *Free Radic Biol Med* 2002;**33**:473-90.
36. Carlsen CU, Kurtmann L, Bruggemann DA, Hoff S, Risbo J, Skibsted LH. Investigation of oxidation in freeze-dried membranes using the

fluorescent probe C11-BODIPY(581/591). *Cryobiology* 2009;**58**:262-7.

37. Ahn WS, Bae SM, Huh SW, Lee JM, Namkoong SE, Han SJ, et al. Necrosis-like death with plasma membrane damage against cervical cancer cells by photodynamic therapy. *Int J Gynecol Cancer* 2004;**14**:475-82.
38. Peeters S, Kitz M, Preisser S, Wetterwald A, Rothen-Rutishauser B, Thalmann GN, et al. Mechanisms of nanoparticle-mediated photomechanical cell damage. *Biomed Opt Express* 2012;**3**:435-46.
39. Catala A. Lipid peroxidation of membrane phospholipids generates hydroxy-alkenals and oxidized phospholipids active in physiological and/or pathological conditions. *Chem Phys Lipids* 2009;**157**:1-11.
40. Acharya A, Ramanujam B, Mitra A, Rao CP. Nanofibers formed through pi…pi stacking of the complexes of glucosyl-C2-salicyl-imine and phenylalanine: characterization by microscopy, modeling by molecular mechanics, and interaction by alpha-helical and beta-sheet proteins. *ACS Nano* 2010;**4**:4061-73.
41. Koren AB, Curtis MD, Francis AH, Kampf JW. Intermolecular interactions in pi-stacked conjugated molecules. Synthesis, structure, and spectral characterization of alkyl bithiazole oligomers. *J Am Chem Soc* 2003;**125**:5040-50.
42. Kato Y, Inoue A, Niidome Y, Nakashima N. Thermodynamics on soluble carbon nanotubes: how do DNA molecules replace surfactants on carbon nanotubes? *Sci Rep* 2012;**2**:733.
43. Zhou Z, Kang H, Clarke ML, Lacerda SH, Zhao M, Fagan JA, et al. Water-soluble DNA-wrapped single-walled carbon-nanotube/quantum-dot complexes. *Small* 2009;**5**:2149-55.
44. Rapozzi V, Miculan M, Xodo LE. Evidence that photoactivated pheophorbide a causes in human cancer cells a photodynamic effect involving lipid peroxidation. *Cancer Biol Ther* 2009;**8**:1318-27.
45. Lavi R, Shainberg A, Friedmann H, Shneyvays V, Rickover O, Eichler M, et al. Low energy visible light induces reactive oxygen species generation and stimulates an increase of intracellular calcium concentration in cardiac cells. *J Biol Chem* 2003;**278**:40917-22.
46. Lavi R, Shainberg A, Shneyvays V, Hochauser E, Isaac A, Zinman T, et al. Detailed analysis of reactive oxygen species induced by visible light in various cell types. *Lasers Surg Med* 2010;**42**:473-80.
47. Gaffney DK, Winter K, Dicker AP, Miller B, Eifel PJ, Ryu J, et al. Efficacy and patterns of failure for locally advanced cancer of the cervix treated with celebrex (celecoxib) and chemoradiotherapy in RTOG 0128. *Int J Radiat Oncol Biol Phys* 2007;**69**:111-7.
48. Lin CS, Jen YM, Cheng MF, Lin YS, Su WF, Hwang JM, et al. Squamous cell carcinoma of the buccal mucosa: an aggressive cancer requiring multimodality treatment. *Head Neck* 2006;**28**:150-7.
49. Ghosh S, Dutta S, Gomes E, Carroll D, D'Agostino Jr R, Olson J, et al. Increased heating efficiency and selective thermal ablation of malignant tissue with DNA-encased multiwalled carbon nanotubes. *ACS Nano* 2009;**3**:2667-73.
50. Shikanov A, Shikanov S, Vaisman B, Golenser J, Domb AJ. Paclitaxel tumor biodistribution and efficacy after intratumoral injection of a biodegradable extended release implant. *Int J Pharm* 2008;**358**:114-20.
51. Shikanov A, Shikanov S, Vaisman B, Golenser J, Domb AJ. Cisplatin tumor biodistribution and efficacy after intratumoral injection of a biodegradable extended release implant. *Chemother Res Pract* 2011;**2011**:175054.
52. Hrkach J, Von Hoff D, Mukkaram Ali M, Andrianova E, Auer J, Campbell T, et al. Preclinical development and clinical translation of a PSMA-targeted docetaxel nanoparticle with a differentiated pharmacological profile. *Sci Transl Med* 2012;**4**:128ra39.
53. Kasten BB, Liu T, Nedrow-Byers JR, Benny PD, Berkman CE. Targeting prostate cancer cells with PSMA inhibitor-guided gold nanoparticles. *Bioorg Med Chem Lett* 2013;**23**:565-8.
54. Fabbro C, Ali-Boucetta H, Da Ros T, Kostarelos K, Bianco A, Prato M. Targeting carbon nanotubes against cancer. *Chem Commun (Camb)* 2012;**48**:3911-26.
55. Liao ZY, Sordet O, Zhang HL, Kohlhagen G, Antony S, Gmeiner WH, et al. A novel polypyrimidine antitumor agent FdUMP[10] induces thymineless death with topoisomerase I-DNA complexes. *Cancer Res* 2005;**65**:4844-51.
56. A.M. Fiorella, Callari L. Luigi Monsù Scolaro, Ludovico Valli and Salvatore Sortino Biocompatible nanoparticles of amphiphilic cyclodextrins entangling porphyrins as suitable vessels for light-induced energy and electron transfer. *J Mater Chem* 2008;**18**:802-5.
57. Meenakshisundaram G, Eteshola E, Pandian RP, Bratasz A, Selvendiran K, Lee SC, et al. Oxygen sensitivity and biocompatibility of an implantable paramagnetic probe for repeated measurements of tissue oxygenation. *Biomed Microdevices* 2009;**11**:817-26.

F10 Inhibits Growth of PC3 Xenografts and Enhances the Effects of Radiation Therapy

William H. Gmeiner[1*], Mark C. Willingham[2], J. Daniel Bourland[3], Heather C. Hatcher[1], Thomas L. Smith[4], Ralph B. D'Agostino Jr.[5], William Blackstock[3]

[1]Department of Cancer Biology, [2]Department of Pathology, [3]Department of Radiation Oncology, [4]Department of Orthopedics, and [5]Department of Public Health Sciences Wake Forest University School of Medicine, Winston-Salem, NC 27157.

*Address Correspondence to this author at:
Phone: (336) 716-6216
Fax: (336) 716-0255
bgmeiner@wfubmc.edu

Running Title: F10 Radiosensitizes PC3 Xenografts

Key Words: Radiosensitization; Prostate Cancer; Fluoropyrimidine; Thymidylate synthase

Abstract

Chemotherapy remains of limited use for the treatment of prostate cancer with only one drug, docetaxel, demonstrating a modest survival advantage for treatment of late-stage disease. Data from the NCI 60 cell line screen indicated that the castration-resistant prostate cancer cell lines PC3 and DU145 were more sensitive than average to the novel polymeric fluoropyrimidine (FP), F10, despite displaying less than average sensitivity to the widely-used FP, 5FU. Here, we show that F10 treatment of PC3 xenografts results in a significant survival advantage (treatment to control ratio (T/C) days =18; $p < 0.001$; $n = 16$) relative to control mice treated with saline. F10 (40 mg/kg/dose) was administered via jugular vein catheterization 3-times per week for five weeks. This aggressive dosing regimen was completed with no drug-induced weight loss and with no evidence of toxicity. F10 was also shown to sensitize PC3 cells to radiation and F10 was also shown to be a potent radiosensitizer of PC3 xenografts *in vivo* with F10 in combination with radiation resulting in significantly greater regression of PC3 xenografts than radiation alone. The results indicate that F10 in this pre-clinical setting is an effective chemotherapeutic agent and possesses significant radiosensitizing properties.

Introduction

Prostate cancer is the most frequently diagnosed cancer in men accounting for nearly one-third of all new malignancies in American men and nearly 30,000 deaths [1]. Chemotherapy has limited utility for the treatment of prostate cancer [2] although docetaxel given in combination with prednisone [3] or estramustine [4] provides a survival benefit for treatment of castration-resistant prostate cancer (CRPC). Docetaxel as an adjuvant to radical prostatectomy also provides a survival advantage for men at high-risk for recurrent disease although treatment caused serious toxicities [5]. There is an urgent need for new and more effective chemotherapeutic options with fewer side effects for prostate cancer patients.

F10 is a novel polymeric fluoropyrimidine (FP) that is under pre-clinical development for treatment of acute myeloid leukemia (AML) [6, 7], glioblastoma (GBM)[8] and other malignancies (Figure 1). The cytotoxic mechanism of F10 involves dual targeting of thymidylate synthase (TS) and DNA topoisomerase 1 (Top1) causing replication-mediated DNA double-strand breaks (DSBs) [9, 10]. Thus, F10 mechanistically resembles the camptothecin (CPT) class of anticancer drugs [11] and is primarily directed towards the DNA locus of FP activity. Results from the NCI-60 cell line screen demonstrated mechanistic similarities to other Top1 poisons but unexpected mechanistic dissimilarities to 5-fluorouracil (5-FU) which is cytotoxic by an RNA-mediated process [9, 10]. The NCI-60 data also showed that the CRPC cell lines PC3 and DU145 cell lines were nearly 1,000-

fold more sensitive to F10 than 5-FU suggesting that F10 might be effective for treating CRPC even though 5-FU and capecitabine (a 5-FU pro-drug) are not [12-14]. F10 is very well-tolerated *in vivo* [6, 8], in part because of high specificity for proliferating cells [7], and may be efficacious without reducing patient quality of life.

In addition to their use in chemotherapy, FPs and Top1 poisons have significant radiosensitizing properties [15, 16]. As radiation therapy is used for treating localized prostate cancer and preventing disease recurrence [17] information on the radiosensitization properties of F10 is important for translational efforts. In this article, we present data showing that F10 inhibits the growth of PC3 xenografts as a single agent and that the combination of F10 and radiation synergistically inhibits growth of PC3 cells in tissue culture and *in vivo*. PC3 cells are derived from bone metastases and have been used as a cellular model of CRPC [18]. We demonstrate that F10 is extremely well-tolerated *in vivo* with much more extensive dosing possible with F10 than with widely-used FPs, such as 5FU. The results obtained indicate that F10 should be evaluated for *in vivo* efficacy and radiosensitization for the clinical treatment of prostate cancer.

Materials and Methods

Cell Culture and Reagents. The human prostate cancer cell line PC3 was obtained from the American Type Culture Collection (Rockville, MD). PC3 cells were cultured at 37 °C in 5% CO_2 atmosphere in RPMI-1640 medium (Gibco/Invitrogen, Carlsbad, CA) supplemented with 10% fetal bovine serum, 2 mM L-glutamine, and 1% penicillin-streptomycin. Cells were passaged every 3 to 5 days upon reaching 80% confluence using 0.25% trypsin/0.05% EDTA. F10 was synthesized and purified under a National Cancer Institute (NCI) contract to support the RAID project. Concentrations of F10 solutions were determined from UV absorption at 260 nm using 30 μg/OD.

TS Catalytic Activity Assays. PC3 cells were plated at a density of 1.5 $x10^6$ cells in 100 mm^2 plates. Cells were grown overnight in RPMI 1640 medium with 10% FBS. Cells were treated with 5-FU or F10 at the indicated concentrations and incubated for 0-48 h, harvested, and lysed by freeze-fracturing. Following centrifugation of cell lysates, supernatants were assayed for protein content and TS catalytic activity as previously described [7].

Clonogenic Assay. PC3 cells were cultured as described above, and were passaged three days prior to plating the cells in 60 x 15 mm Petri dishes for the clonogenic assays. Cells at 500 and 750 cells/mL were plated for F10 concentrations of 10^{-10} to 10^{-6} M while 250 and 500 cell/mL were plated for 5-FU concentrations from 10^{-8} to 10^{-5} M. Cells were allowed to attach for 24 h prior to treatment for 72 h. Each experiment was done in duplicate. The mean value and standard deviation were determined for each drug concentration. Following treatment, the medium was removed and replaced with fresh medium. Cells were then incubated for seven days, and stained with crystal violet. Colonies were counted manually, with a minimal colony diameter of approximately 1 mm required for counting.

Radiation Enhancement. The effects of F10 on the response of PC3 cells to radiation were also evaluated using clonogenic assay. PC3 cells were plated as described above for F10-only treatment at densities of 200 and 400 cells/mL (0 Gy), 400 and 800 cells/mL (2 Gy), 800 and 1,600 cells/mL (4 Gy), 1,600 and 3,200 cells/mL (6 Gy) and 3,200 and 6,400 cells/mL (8 Gy). Cells were incubated with F10 for 24 h and then irradiated using a 300 kV orthovoltage X-Ray irradiator (Precision X-Ray, incorporated, North Brantford, CT). Following irradiation, cells were further incubated to complete the entire drug exposure period of 72 h. The surviving fraction was normalized to F10-only treatment to determine to what extent F10 enhanced radiation-mediated cytotoxicity apart from drug-induced effects.

Jugular Vein Catheterization. Male NCr Nude (*nu/nu*) mice were purchased from The National Cancer Institute (Bethesda, MD) and maintained in a WFSM animal facility. All treatments and procedures in mice were conducted according to guidelines approved by the Animal Care and Use Committee of Wake Forest University Health Sciences. Prior to tumor inoculation, polyethylene tubing (PE10) was used to cannulate the jugular vein of mice seven weeks of age. The portion of the catheter, which exited through the animal's skin, was 4-5 cm in length, allowing multiple procedures during the course of the study. Catheters were supplied with a heparin lock and heat-sealed following each procedure. A two component, cloth-covered button kit was used to contain and protect the portion of the catheter outside the mouse. The button was sewn to the mid-scapular region on the mouse's back with the base attached to the mouse and the heat-sealed catheter protected by a cap. For each saline or drug injection, the cap was removed, the catheter was wiped with an alcohol pad and the heat seal removed with a sterile blade. A 30-gauge needle was used to flush the line first with heparinized saline, followed by administration of saline or drug, and followed with a heparin lock and heat-sealing. All injections and all irradiation procedures were carried out with the mice anesthetized with isoflurane. Mice were placed in a Plexiglass induction chamber (25 x 11 x 12 cm) that was filled with 2% isoflurane in O_2. Pedal reflex was tested when the mice showed no eye-blink response when the chamber was tapped (~2 min). Anesthesia was maintained through voluntary breathing of a mixture of 1.5 – 2% isofluorane in O_2.

Establishment of tumor xenografts and *in vivo* experiments. The human prostate cancer cell line PC3 was grown to 80% confluence and harvested. Cells were re-suspended in serum-free RPMI-1640 medium with penicillin and streptomycin, mixed 1:1 with Growth Factor Reduced (GFR) BD Matrigel Basement Membrane Matrix (BD Biosciences, Palo Alto, California). Using a cold syringe and 27-gauge needle, 3.5 x 10^6 cells were injected subcutaneously into each lateral flank of male athymic *nu/nu* mice 8 weeks of age. At two weeks post-inoculation, palpable tumors (~500 mm^3) were established and animals were randomized into control and treatment arms consisting of eight to nine animals, respectively, with the latter receiving 40 mg/kg body weight F10 in 100 μL of sterile saline intravenously via jugular vein catheters beginning on Day 0 and alternating with orthovoltage (X-Ray) radiation every 24 hours for five days and continuing each week for 5 weeks. An irradiation schedule of 30 Gy in 10 fractions of 3 Gy each over a 5-week period was used (2 fractions per week), delivered using a 300 kV orthovoltage X-Ray irradiator (Precision X-Ray, incorporated, North Brantford, CT). This irradiation schedule is equivalent to a fractionated dose regimen of approximately 36 Gy in 18 fractions of 2 Gy each or a single fraction of 12-15 Gy. Animal weights were measured each week, and perpendicular tumor diameters were measured using a Vernier scale caliper twice per week until animals were sacrificed, at which time tumors and tissues were harvested. Tumor volume was estimated using the formula: $\pi/6$ x length x width x thickness. Animals were euthanized and tumors and other tissues were removed when tumor volume in a single flank exceeded 3000 mm^3. Sections of the tumor were fixed in fresh 10% neutral buffered formaldehyde before embedding in paraffin for hematoxylin and eosin staining.

Statistical Methods. Survival data and tumor growth curves were compared between groups using parametric and non-parametric methods (i.e. Kaplan-Meier curves and log-rank tests) using SAS (Version 9, Cary, NC). Mean tumor volumes and SE values are shown in figures for comparison and to show trends. Comparisons between the four groups (drug +/- radiation; saline +/- radiation) were made using repeated measures mixed model analysis where mice were considered as random effects and day, group and the day by group interaction were included as fixed effects. The day by group interaction was examined to determine whether the four groups had different changes in tumor volumes over time. In addition to this interaction test, we compared the mean values at different time points to determine at which time longitudinally the four groups began to differ from each other. Median and ranges of tumor volumes at a given date were calculated to determine T/C ratios and these median volume scores were compared using non-parametric two-sample median tests. Survival curves were generated to compare groups and since all animals died at some time during the experiment mean survival times could be compared using two-sample t-tests (i.e. there were no censored data), as well as the median survival times (via the log-rank test).

RESULTS

F10 Inhibits Clonogenic Survival. The NCI-60 data indicated the CRPC cell lines PC3 and DU145 were highly sensitive to F10 with GI_{50} values in the nanomolar range. To evaluate the cytotoxicity of F10 towards PC3 cells, we performed clonogenic assays (Figure 1). Treatment with F10 at 100 nM reduced PC3 clonogenic survival >50% while at 1 μM F10 completely inhibited PC3 cell colony formation. In contrast to the results obtained with F10, 5-FU had minimal effect on the clonogenic potential of PC3 cells. Treatment with 1 μM 5FU had no effect on PC3 cell colony formation and even 10 μM 5-FU did not decrease colony formation by 50%. These results are consistent with clinical studies demonstrating that 5-FU is unlikely to be effective for treating prostate cancer but demonstrate that F10 is substantially more potent and should be considered for prostate cancer treatment.

F10 is a Potent Inhibitor of TS. Thymidylate synthase (TS) is a principal target of fluoropyrimidine (FP) chemotherapy and inhibiting TS is considered central to the anti-tumor activity of FP drugs. We evaluated TS catalytic activity in PC3 cells following treatment with either 5-FU or F10 (Figure 1). F10 significantly reduced TS activity relative to control within 8 h and TS activity remained significantly decreased through 72 h. In contrast 5FU treatment had minimal effect on reducing TS activity with activity levels actually increased at 8 and 16 h for 5-FU treatment relative to control and only the 48 h timepoint showing a significant decrease (~50% control).

F10 Enhances the Effects of Radiation. We next evaluated to what extent F10 enhanced the effects of radiation at inhibiting the clonogenic survival of PC3 cells (Figure 2). Radiation-only was also effective at reducing colony formation of PC3 cells with 2 Gy reducing colonies to ~50% control. For all doses of radiation evaluated F10 co-treatment significantly decreased clonogenic potential (Figure 2A). For example 100 nM F10 decreased colony formation at 2 Gy from 50% to 20%. When the data were normalized to separate the F10-only cytotoxic effects from the effects of radiation (Figure 2B) a true radiosensitization effect was apparent for F10. Thus, F10 has potential to be used both for direct anti-tumor effects as well as radiosensitization for treatment of prostate cancer.

F10 Inhibits PC3 Tumor Growth and Increases Survival

The antitumor activity of F10 was evaluated in NCR nu/nu mice in which PC3 tumor cells had been implanted 14 days previously. Mean initial tumor volumes were approximately 500 mm^3. Mice treated with F10 had significantly longer survival times relative to saline-treated controls. The mean survival time for mice treated with F10 was 66 days while the mean survival time for saline-treated control animals was 48 days. Thus, treatment with F10 resulted in increased survival of 18 days (T/C days =18; $p < 0.001$; n = 16 – Figure 3). In all cases, mice were removed from the study as a result of tumor burden in the non-irradiated flank, thus survival is a direct comparison of the ability of F10 alone to reduce tumor growth. Median survival times were also significantly increased as a result of F10 treatment ($p < 0.002$; n = 16).

The repeated measures mixed model indicated that there were significant group by day interactions suggesting that the tumor volumes were changing at different rates in the four treatment groups (saline (S); F10 (F); S + radiation (R); and F10 + radiation (F+R). The non-irradiated groups (F and S) began to differ starting at day 20 while the irradiated and non-irradiated (Saline) and the irradiated and non-irradiated (F10) groups began differing significantly at Day 17 (Figure 3). When we compared the median tumor volumes between groups we found using one-tailed comparisons that by day 24 there were significant differences between all groups. The F-irradiated group (F+R) differed from the S-non-irradiated group (S) (p=.002; n = 16), F-non-irradiated (F) versus S-non-irradiated (S) (p=.026; n = 16), and S-irradiated (R) versus S-non-irradiated (S) (p=.0018; n = 16). Although the growth trends clearly indicated continued differentiation among tumor size in the four treatment groups, animals with the largest tumors in the saline group were euthanized due to tumor burden in the non-irradiated flank and direct comparisons among treatment groups were not possible at later timepoints.

Treatment with F10 did not result in weight loss significantly greater than mice treated with vehicle-only. The weight loss in the F10-treated mice was greatest on day 14 with a mean weight loss of 11%. Saline-treated animals had a mean weight loss of 8% at day 14 and a mean weight loss of 11% on day 28 (Figure 4). The weight loss displayed in both the drug-treated and non-drug-treated mice likely resulted from the effects of the anesthesia (isoflurane) that was administered daily prior to either drug-injection or irradiation. The F10-treated mice quickly adjusted to the treatment protocol and began re-gaining weight during the third week of treatment. In contrast, the saline-treated control group continued to lose weight as tumor burden increased in these animals. The present results confirm that extended treatment with F10 is very well-tolerated *in vivo* and does not result in significant weight-loss at efficacious doses.

Histological examination of tissues from animals sacrificed at the conclusion of the study revealed no toxicity to the gastrointestinal tract or to other tissues of drug-treated mice (Figure 4). Mice-treated with F10 also displayed no signs of neutropenia as assessed by histological examination of a cross-section of the femur (data not shown). Other tissues examined included liver, lungs, and kidneys. There was no sign of drug-related toxicity in any tissues. Thus, our results indicate that F10 at a concentration of 40 mg/kg/dose significantly reduces tumor growth; furthermore, doses that are higher than those administered in the present study are likely to be well-tolerated *in vivo*. Since a dose-response is evident for PC3 cells in culture, it is possible that an even greater reduction in tumor burden could be achieved with higher dosage.

The Combination of F10 and Radiation Potently Reduces Tumor Burden

The antitumor activity of F10 in combination with radiation was compared to radiation only, drug-treatment alone, and no treatment by analyzing the growth curves for the left-flank tumors of mice treated with F10 relative to the other tumor groups (Figure 3). The growth rates for tumors treated with F10 + radiation were significantly less than for tumors treated with radiation-only, drug-only, or saline control. The tumor growth delay (T/C% = 21%) for the F10 + radiation group was significantly reduced relative to control ($p < 0.005$; $n = 16$). The tumor growth delay for radiation only was also significant relative to control (T/C% = 36%; $p < 0.05$; $n = 16$). The radiation-sensitizing properties of F10 were apparent in comparison of the F10 + radiation group to radiation alone ($p < 0.01$; $n = 16$).

Although the study design did not permit direct comparison with respect to survival of mice treated with F10 + radiation relative to radiation-only and to drug-only, the final tumor sizes for PC3 xenografts treated with F10 + radiation were significantly smaller, on average, than were the final tumor sizes for PC3 xenografts treated with radiation only (Figure 4). Measurement of final tumor size for the F10 + radiation PC3 xenografts occurred an average of 18 days later than for xenografts treated with radiation-only, as euthanasia of animals was required based on tumor volume for the non-irradiated flank. Average tumor volumes did not become significantly larger for the tumors treated with F10 + radiation during the final weeks of the study indicating that the combination had a long-term effect on tumor growth and animal survival. Histological examination of tumors treated with F10 + radiation revealed marked hypocellularity of the excised tissue (Figure 5). The results indicate that F10 is a potent radiosensitizer and that the combination of F10 + radiation may be highly effective for the treatment of prostate cancer. Histological examination of tumors from the non-irradiated flank of saline-treated and F10-treated mice revealed marked necrosis in the saline-treated animals, but not the F10-treated mice which were euthanized, on average, 18 days later. The results are consistent with tumor re-growth following the conclusion of F10 administration on day 33 (Figure 3).

Discussion

Advanced prostate cancer remains a challenging disease with few effective chemotherapeutic options. Our studies show the novel FP F10 increases survival of mice with PC3 xenografts and sensitizes PC3 xenografts to radiation. These results are somewhat unexpected in light of previous studies reporting that 5-FU and capecitabine are not efficacious for treating prostate cancer [12-14] and likely reflects selective targeting of the DNA-directed locus of FP activity. Thus, F10 may be effective in the clinical management of prostate cancer both as a chemotherapeutic agent and as a radiosensitizer.

The results of the present study stand in stark contrast to previous studies with 5-FU that determined the maximum tolerated dose of 5-FU to be 45 mg/kg/dose on a once daily, three times per week dosing schedule with higher doses resulting in lethality. In the present study, we were able to continue dosing with F10 at 40 mg/kg/dose 3-times per week for 5 consecutive weeks with no adverse drug-related effects. Animals in the F10-treated group experienced no drug-induced weight loss and histological examination of the GI-tract following animal sacrifice at the end of the study indicated no drug-related damage to the GI-tract or any other tissues. These results are consistent with the GI-tract toxicity of FPs being mainly an RNA-mediated effect [19] and indicate that selectively targeting the DNA-directed locus of FP activity with F10 results in significant antitumor activity and with elimination of the GI-tract toxicity associated with 5-FU treatment. The lack of toxicity at the current dose indicates that higher or more extensive dosing than was employed in the present study is likely to be safe. In light of the observed concentration-dependence of F10 cytotoxicity and radiosensitization, higher dosing may further reduce tumor burden *in vivo*.

The radiosensitization properties of FPs and Top1 poisons have been documented [15, 16]. The extent of radiosensitization observed with F10 in the present study compares favorably with Gossypol [18] and curcumin [20] – two natural products that are being evaluated as radiosensitizers for the treatment of prostate cancer and other malignancies. F10 displays strong anticancer activity as a single agent, is radiosensitizing, and is very well tolerated *in vivo*. While chemically and mechanistically distinct from conventional FPs, F10 has similarities to these drugs that have been used successfully in the clinic for decades. Future clinical studies can draw upon this longstanding clinical experience as well as new mechanistic insights obtained with this novel FP polymer.

Acknowledgements. This work was supported by DOD PCRP 093606, DOD PCRP 110135, NIH CA102532, NIH P30 CA12197 and the NCI RAID Program. The authors are grateful for technical assistance from Jamie Jennings-Gee, Christopher Stuart, and Stacey Trozzo.

References

1. ACS Facts and Figures, 2013.
2. Hadaschik, B.A., R.D. Sowery, and M.E. Gleave, *Novel targets and approaches in advanced prostate cancer.* Curr Opin Urol, 2007. **17**(3): p. 182-7.
3. Tannock, I.F., R. de Wit, W.R. Berry, J. Horti, A. Pluzanska, K.N. Chi, S. Oudard, C. Theodore, N.D. James, I. Turesson, M.A. Rosenthal, and M.A. Eisenberger, *Docetaxel plus prednisone or mitoxantrone plus prednisone for advanced prostate cancer.* N Engl J Med, 2004. **351**(15): p. 1502-12.
4. Petrylak, D.P., C.M. Tangen, M.H. Hussain, P.N. Lara, Jr., J.A. Jones, M.E. Taplin, P.A. Burch, D. Berry, C. Moinpour, M. Kohli, M.C. Benson, E.J. Small, D. Raghavan, and E.D. Crawford, *Docetaxel and estramustine compared with mitoxantrone and prednisone for advanced refractory prostate cancer.* N Engl J Med, 2004. **351**(15): p. 1513-20.
5. Kibel, A.S., E. Rosenbaum, M.W. Kattan, J. Picus, R. Dreicer, E.A. Klein, G.S. Chatta, J.B. Nelson, R.S. DiPaola, B.J. Roth, M.S. Cookson, G. Wilding, D.F. Jarrard, T.M. Beer, C.W. Ryan, D.P. Petrylak, M.C. Benson, A.W. Partin, E. Garrett-Mayer, and M.A. Eisenberger, *Adjuvant weekly docetaxel for patients with high risk prostate cancer after radical prostatectomy: a multi-institutional pilot study.* J Urol, 2007. **177**(5): p. 1777-81.
6. Pardee, T.S., Gomes, E., Jennings-Gee, J., Caudell, D., Gmeiner, W.H., *Unique dual targeting of thymidylate synthase and topoisomerase 1 by FdUMP[10] results in high efficacy against AML and low toxicity.* Blood, 2012. **119**: p. 3561-3570.
7. Jennings-Gee, J., Pardee, TS, Gmeiner, WH, *Replication-dependent irreversible topoisomerase 1 poisoning is responsible for FdUMP[10] anti-leukemic activity.* Exp Hematol, 2013. **PMID: 23085462**.
8. Gmeiner, W.H., C. Lema-Tome, D. Gibo, J. Jennings-Gee, C. Milligan, and W. Debinski, *Selective anti-tumor activity of the novel fluoropyrimidine polymer F10 towards G48a orthotopic GBM tumors.* J Neurooncol, 2014. **116**(3): p. 447-54.
9. Gmeiner, W.H., W.C. Reinhold, and Y. Pommier, *Genome-wide mRNA and microRNA profiling of the NCI 60 cell-line screen and comparison of FdUMP[10] with fluorouracil, floxuridine, and topoisomerase 1 poisons.* Mol Cancer Ther, 2010. **9**(12): p. 3105-14.

10. Liao, Z.Y., O. Sordet, H.L. Zhang, G. Kohlhagen, S. Antony, W.H. Gmeiner, and Y. Pommier, *A novel polypyrimidine antitumor agent FdUMP[10] induces thymineless death with topoisomerase I-DNA complexes.* Cancer Res, 2005. **65**(11): p. 4844-51.
11. Pommier, Y., E. Leo, H. Zhang, and C. Marchand, *DNA topoisomerases and their poisoning by anticancer and antibacterial drugs.* Chem Biol, 2010. **17**(5): p. 421-33.
12. Berlin, J.D., K.J. Propert, D. Trump, G. Wilding, G. Hudes, J. Glick, P. Burch, A. Keller, and P. Loehrer, *5-Fluorouracil and leucovorin therapy in patients with hormone refractory prostate cancer: an Eastern Cooperative Oncology Group phase II study (E1889).* Am J Clin Oncol, 1998. **21**(2): p. 171-6.
13. Huan, S.D., S.E. Aitken, and D.J. Stewart, *A phase II study of 5-fluorouracil and high dose folinic acid in cisplatin-refractory metastatic bladder cancer.* Ann Oncol, 1995. **6**(8): p. 836-7.
14. Morant, R., J. Bernhard, D. Dietrich, S. Gillessen, M. Bonomo, M. Borner, J. Bauer, T. Cerny, C. Rochlitz, M. Wernli, A. Gschwend, S. Hanselmann, F. Hering, and H.P. Schmid, *Capecitabine in hormone-resistant metastatic prostatic carcinoma - a phase II trial.* Br J Cancer, 2004. **90**(7): p. 1312-7.
15. Lawrence, T.S., M.A. Davis, H.Y. Tang, and J. Maybaum, *Fluorodeoxyuridine-mediated cytotoxicity and radiosensitization require S phase progression.* Int J Radiat Biol, 1996. **70**(3): p. 273-80.
16. Chen, A.Y., R. Chou, S.J. Shih, D. Lau, and D. Gandara, *Enhancement of radiotherapy with DNA topoisomerase I-targeted drugs.* Crit Rev Oncol Hematol, 2004. **50**(2): p. 111-9.
17. Sailer, S.L., *Radiation therapy for prostate cancer: external beam, brachytherapy, and salvage.* N C Med J, 2006. **67**(2): p. 149-53.
18. Xu, L., D. Yang, S. Wang, W. Tang, M. Liu, M. Davis, J. Chen, J.M. Rae, T. Lawrence, and M.E. Lippman, *(-)-Gossypol enhances response to radiation therapy and results in tumor regression of human prostate cancer.* Mol Cancer Ther, 2005. **4**(2): p. 197-205.
19. Pritchard, D.M., A.J. Watson, C.S. Potten, A.L. Jackman, and J.A. Hickman, *Inhibition by uridine but not thymidine of p53-dependent intestinal apoptosis initiated by 5-fluorouracil: evidence for the involvement of RNA perturbation.* Proc Natl Acad Sci U S A, 1997. **94**(5): p. 1795-9.
20. Chendil, D., R.S. Ranga, D. Meigooni, S. Sathishkumar, and M.M. Ahmed, *Curcumin confers radiosensitizing effect in prostate cancer cell line PC-3.* Oncogene, 2004. **23**(8): p. 1599-607.

Figure Legends

Figure 1. F10 strongly inhibits the clonogenicity of PC3 cells. (*A*) Structure of F10. (*B*) Clonogenic survival assay evaluating clonogenic survival of PC3 cells following 72 h treatment with either F10 or 5-FU at the indicated concentration (nM). No surviving colonies were observed following treatment with F10 at 1 μM (1,000 nM). In contrast, treatment with 5FU at 10 μM (10,000 nM) decreased the percent of colonies surviving relative to control by less than 50%. (*C*) TS activity in PC3 cells at the indicated times following treatment with F10 (10^{-8} M) or 5-FU (10^{-6} M) (* $p < 0.05$ vs control based on Student's two sided t-test).

Figure 2. Results of a clonogenic assay evaluating the survival fraction of PC3 cells exposed to radiation or radiation in combination with F10. (*A*) Graph of surviving fraction as a percent of non-treated cells. (*B*) Same data as in (A) but normalized for F10-only effects to determine if F10 were radiosensitizing. (* $p < 0.05$ vs control based on Student's two sided t-test).

Figure 3. Treatment with F10 significantly reduces the growth of established PC3 cell xenografts. (*A*) Tumor growth curves for the four tumor groups in the study (left and right flank tumors from each treatment group were analyzed separately). Error bars indicate +/-SEM, n = 8. (*B*) A typical mouse in the study. Tumors were initiated by s.c. injection of PC3 cells bilaterally. Initial tumor volumes were approximately 500 mm^3 in all treatment groups. The left flank tumor in each mouse was selectively irradiated using the orthovoltage X-ray

irradiator (GE Healthcare). (*C*) Treatment schedule for the *in vivo* experiment. Mice were assigned to one of two treatment groups – either F10 at 40 mg/kg dissolved in 100 μL of sterile saline or saline-only. Treatment was administered through a catheter inserted into the jugular vein. Drug was administered 3x per week for five weeks on the days indicated. A dose of 3 Gy radiation was administered to the left flank of all animals 2x per week for five weeks on the indicated days. (D) Kaplan-Meier survival curves for mice treated with F10 or with saline control. Mice were removed from the study based on tumor size in the non-irradiated flank.

Figure 4. F10 treatment does not result in weight loss greater than control treatment or cause damage to the colonic epithelium. Also, the combination of F10 + radiation results in significantly smaller final tumor size relative to treatment with radiation alone. (*A*) Average weights for F10-treated and control mice. Error bars indicate +/-SEM, n = 8. (*B*) Graph of the final mean tumor volumes for left-flank tumors in the study. Tumors treated with F10 + irradiation were significantly smaller than tumors treated with radiation. Graph depicts the mean +/- SEM (n = 8) for left flank tumors from the F10-treated and saline groups. (*C*) H&E section (10x) of colonic epithelium from an F10-treated mouse. (*D*) Colonic epithelium from a saline-treated mouse. Both mice were sacrificed as a result of tumor burden to the non-irradiated flank. There is no deterioration of the colonic epithelium in mice from treated with F10.

Figure 5. H&E sections (4x) from a left-flank (irradiated) tumor from an (*A*) F10-treated animal; and (*B*) Saline-treated animal. Irradiated tumors from the F10-treated group displayed marked hypocellularity relative to saline-treated animals. (*C*) H&E section from the right-flank (non-irradiated) tumor from an F10-treated animal and (*D*) from the right-flank of a saline-treated animal. While animals from both groups were sacrificed based on volumes in the right-flank tumors, tumors from the saline group displayed marked necrosis. Animals from the F10-treated group were sacrificed, on average, 18 days later than animals in the saline group (see Figure 3).

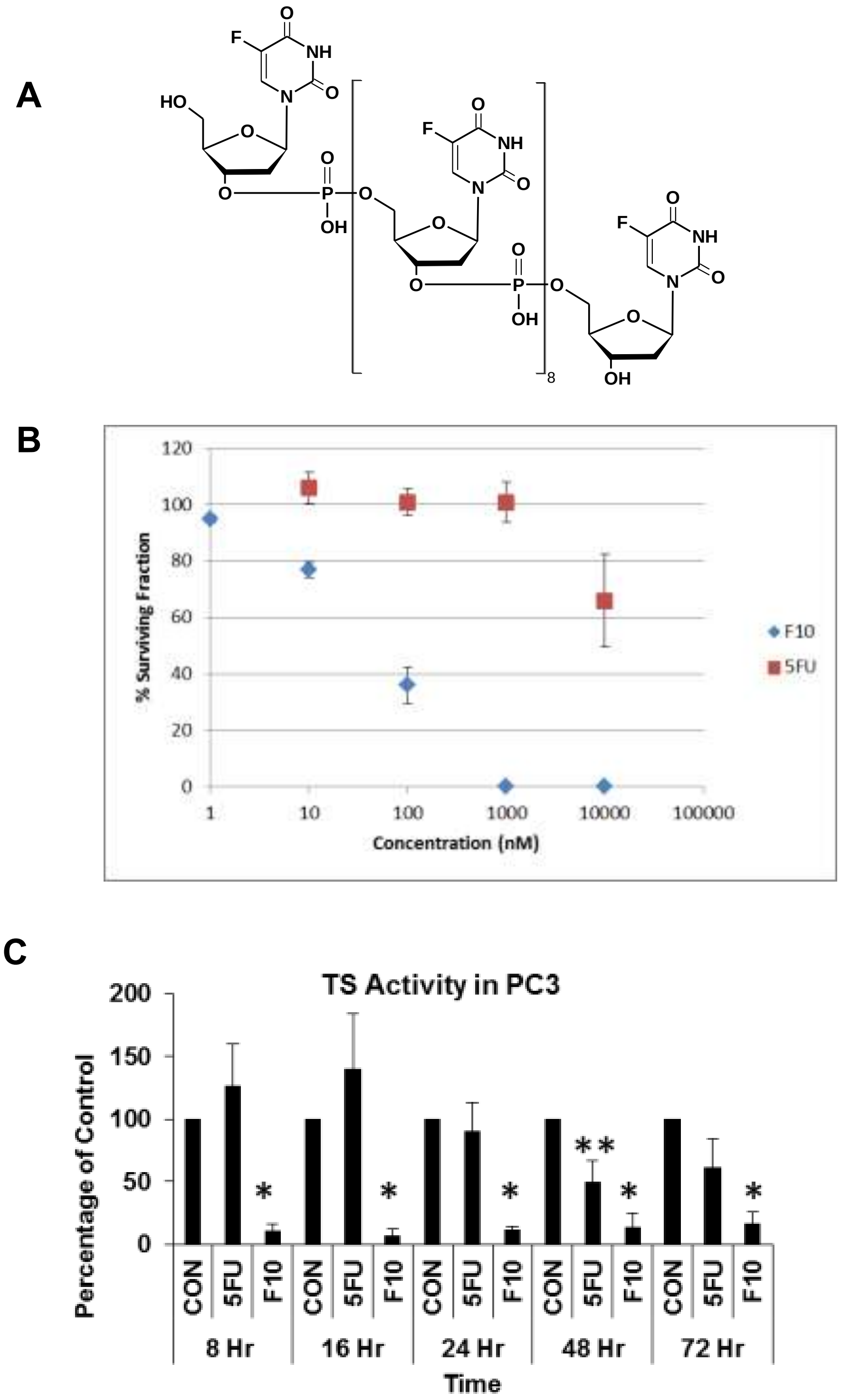
A
F
O
NH
N
O
HO
O
O
P
O
OH
O
8
OH
B
120
100
80
60
40
20
0
% Surviving Fraction
1
10
100
1000
10000
100000
Concentration (nM)
◆ F10
■ 5FU
C
TS Activity in PC3
200
150
100
50
0
Percentage of Control
*
**
CON
5FU
F10
8 Hr
16 Hr
24 Hr
48 Hr
72 Hr
Time

Figure 1

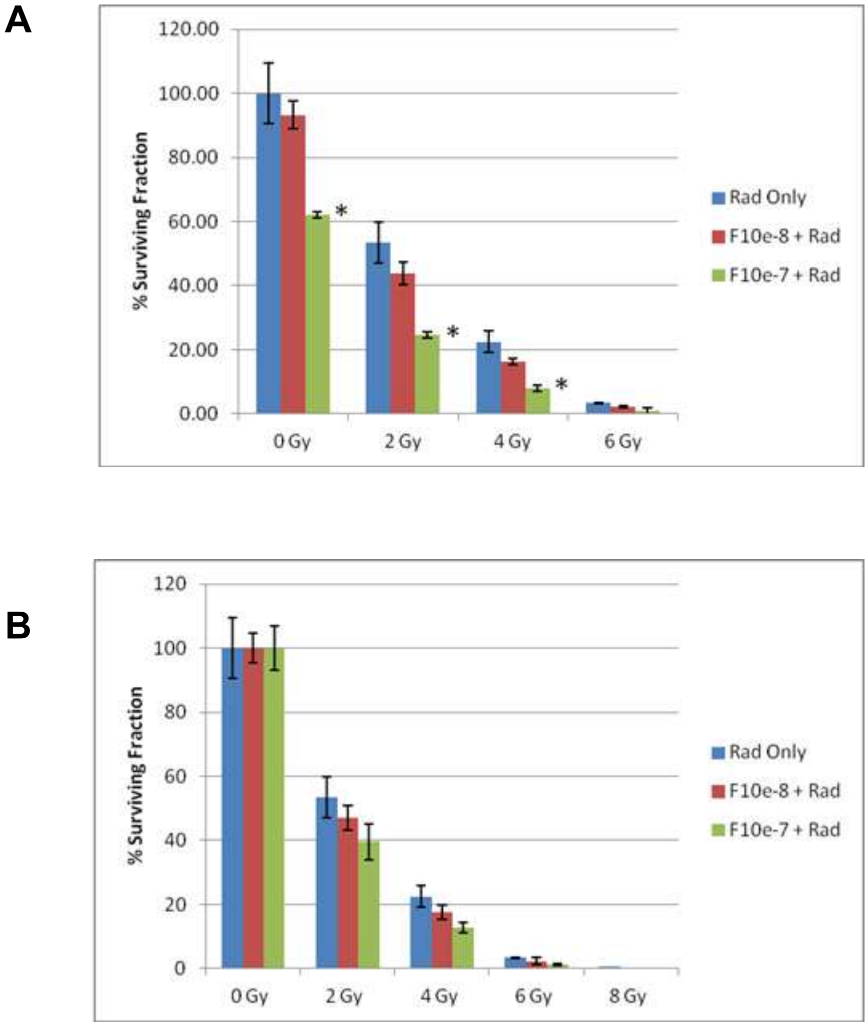
A
120.00
100.00
80.00
60.00
40.00
20.00
0.00
% Surviving Fraction
*
*
*
0 Gy
2 Gy
4 Gy
6 Gy
Rad Only
F10e-8 + Rad
F10e-7 + Rad
B
120
100
80
60
40
20
0
% Surviving Fraction
0 Gy
2 Gy
4 Gy
6 Gy
8 Gy
Rad Only
F10e-8 + Rad
F10e-7 + Rad

Figure 2

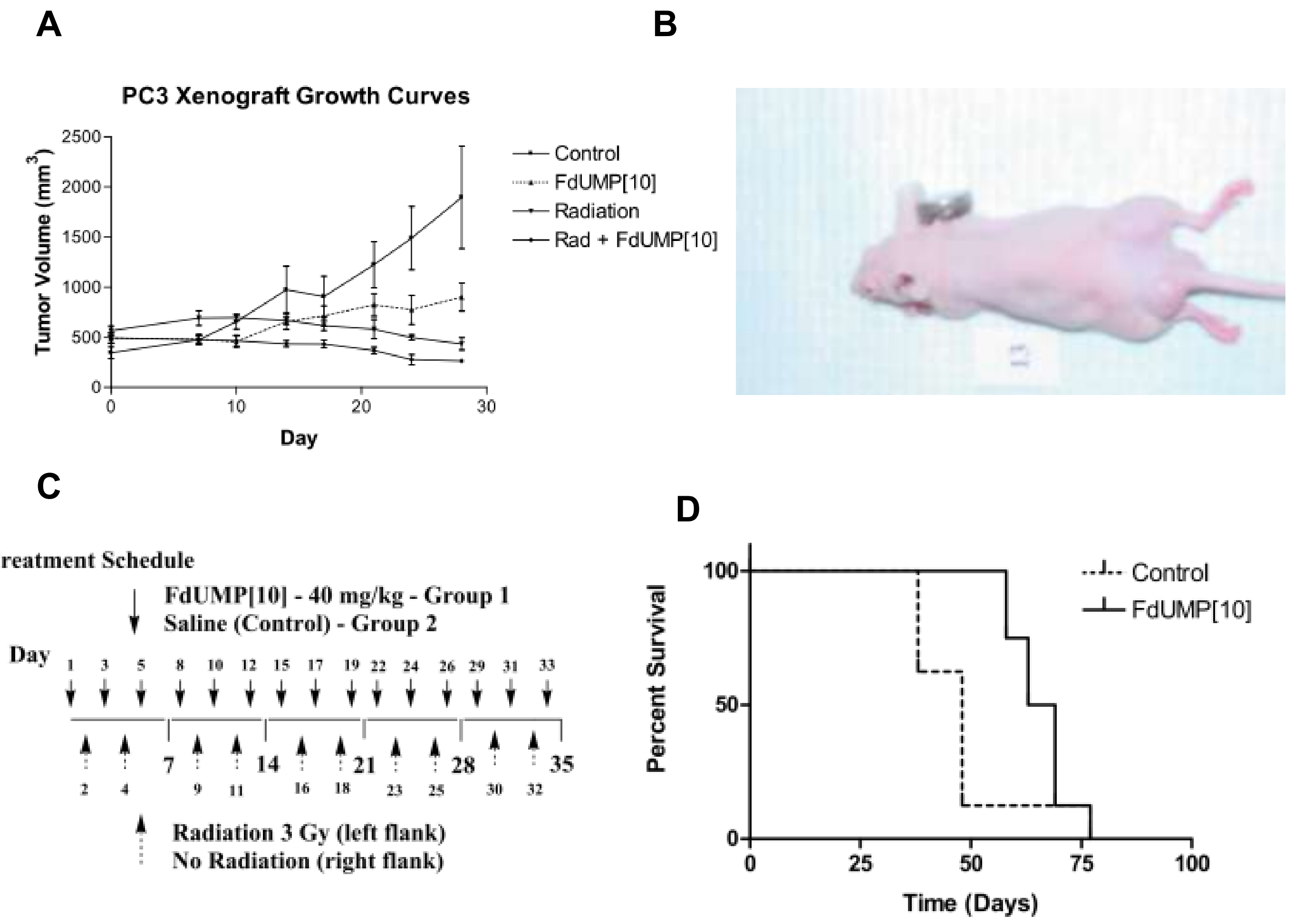
A
B
C
D
PC3 Xenograft Growth Curves
Tumor Volume (mm^3)
2500
2000
1500
1000
500
0
Day
0
10
20
30
Control
FdUMP[10]
Radiation
Rad + FdUMP[10]
Treatment Schedule
FdUMP[10] - 40 mg/kg - Group 1
Saline (Control) - Group 2
Day
1 3 5 8 10 12 15 17 19 22 24 26 29 31 33
7 14 21 28 35
2 4 9 11 16 18 23 25 30 32
Radiation 3 Gy (left flank)
No Radiation (right flank)
Percent Survival
100
50
0
Time (Days)
0
25
50
75
100
Control
FdUMP[10]

Figure 3

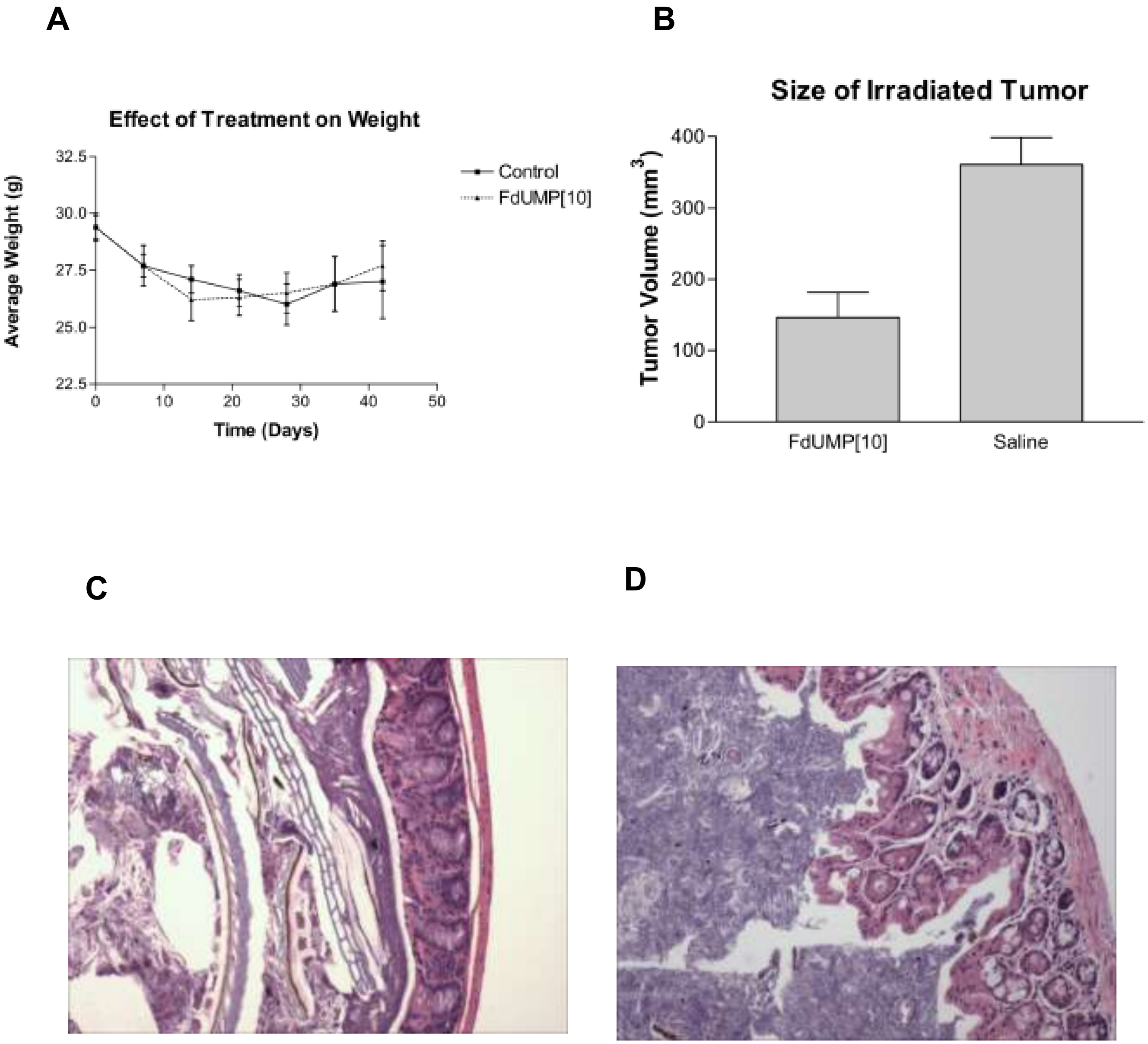
A
Effect of Treatment on Weight
Average Weight (g)
32.5
30.0
27.5
25.0
22.5
0
10
20
30
40
50
Time (Days)
Control
FdUMP[10]
B
Size of Irradiated Tumor
Tumor Volume (mm^3)
400
300
200
100
0
FdUMP[10]
Saline
C
D

Figure 4

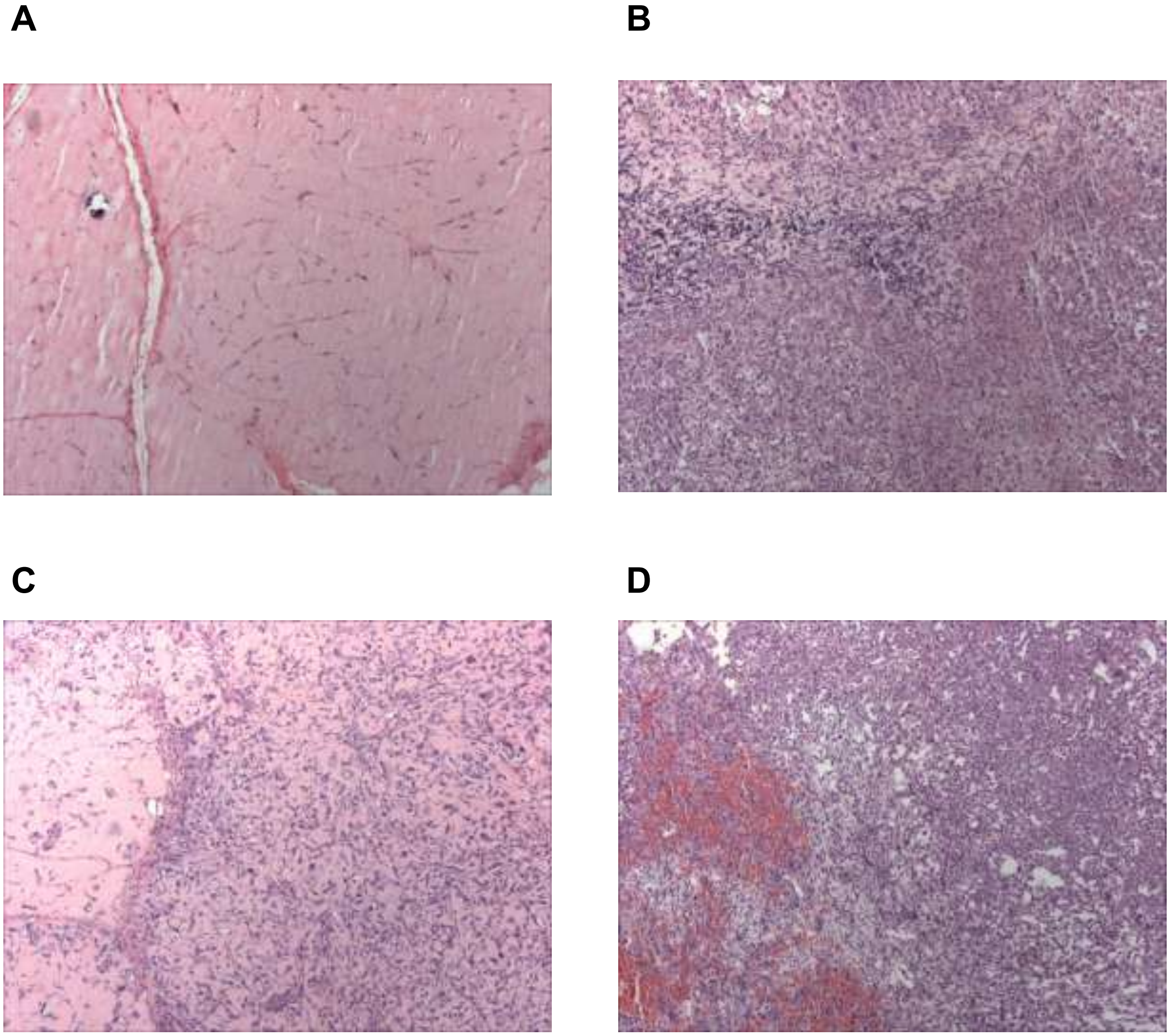

Figure 5

Bioconjugate Chemistry

Article

pubs.acs.org/bc

Site-Specific DNA–Doxorubicin Conjugates Display Enhanced Cytotoxicity to Breast Cancer Cells

Christopher H. Stuart,[†,‡] David A. Horita,[§,⊥] Michael J. Thomas,[§] Freddie R. Salsbury, Jr.,[∥]
Mark O. Lively,[§] and William H. Gmeiner*[,†,‡]

[†]Department of Cancer Biology, [‡]Department of Molecular Medicine and Translation Science, Wake Forest School of Medicine, and
[§]Department of Biochemistry, Wake Forest School of Medicine, Winston-Salem, North Carolina 27157, United States
[∥]Department of Physics, Wake Forest University, Winston-Salem, North Carolina 27109, United States

Supporting Information

ABSTRACT: Doxorubicin (Dox) is widely used for breast cancer treatment but causes serious side effects including cardiotoxicity that may adversely impact patient lifespan even if treatment is successful. Herein, we describe selective conjugation of Dox to a single site in a DNA hairpin resulting in a highly stable complex that enables Dox to be used more effectively. Selective conjugation of Dox to G15 in the hairpin loop was verified using site-specific labeling with [2-^{15}N]-2′-deoxyguanosine in conjunction with [^{1}H–^{15}N] 2D NMR, while 1:1 stoichiometry for the conjugate was validated by ESI-QTOF mass spectrometry and UV spectroscopy. Molecular modeling indicated covalently bound Dox also intercalated into the stem of the hairpin and stability studies demonstrated the resulting Dox-conjugated hairpin (DCH) complex had a half-life >30 h, considerably longer than alternative covalent and noncovalent complexes. Secondary conjugation of DCH with folic acid (FA) resulted in increased internalization into breast cancer cells. The dual conjugate, DCH-FA, can be used for safer and more effective chemotherapy with Dox and this conjugation strategy can be expanded to include additional anticancer drugs.

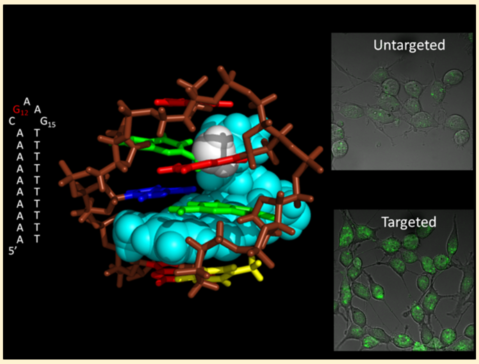

INTRODUCTION

Doxorubicin (Dox) is widely used for treating breast cancer and other malignancies; however, serious toxicities, including an occasionally lethal cardiotoxicity, counter the therapeutic benefit of Dox, resulting in a search for chemical modifications that attenuate systemic toxicities while maintaining strong antitumor activity.[1] The principal cytotoxic mechanism of Dox is poisoning of DNA topoisomerase 2 (Top2) which results in generation of lethal DNA double strand breaks (DSBs).[2] Dox also undergoes REDOX cycling and increases oxidative stress following cell uptake. Recent studies have indicated that Dox cardiotoxicity results from an on-target effect, the poisoning of Top 2 in cardiomyocytes.[3] Hence, strategies to improve the therapeutic index of Dox require prolonged sequestration of Dox while in circulation and efficient Dox release following selective uptake into targeted cancer cells. We describe here a new approach for Dox delivery to cancer cells that takes advantage of the selective chemical reactivity of a single-site in a DNA hairpin to create a novel Dox-conjugated DNA hairpin (DCH) with favorable Dox retention and release properties and that is targeted to breast cancer cells via folic acid conjugation.

DNA is central to biological function as the repository of genetic information, but DNA also has tremendous potential as a material with diverse potential functions, including drug delivery. Our laboratory has demonstrated the utility of DNA for delivery of cytotoxic nucleotide analogs with F10, a polymer of the thymidylate synthase (TS) inhibitory nucleotide 5-fluoro-2′-deoxyuridine-5′-*O*-monophosphate (FdUMP) displaying enhanced antileukemic activity and reduced systemic toxicity relative to conventional fluoropyrimidine drugs such as 5-fluorouracil (5-FU).[4,5] We recently demonstrated the potential for DNA hairpins to be useful for drug delivery with involvement of both the major and minor grooves as well as the duplex region of the hairpin. We have shown that cytotoxicity can be modulated by inclusion of minor groove binding ligands, such as netropsin or distamycin, while Zn^{2+}, a metal ion that displays anticancer activity, can occupy the major groove in DNA hairpins appropriately substituted with FdU nucleotides in the stem.[6,7] Hence, not only are the chemical properties of DNA of potential use for drug delivery, but its structural diversity may also be utilized for drug delivery applications.

Dox interacts with DNA via intercalation of the tetracene ring system between the planar base pairs of duplex DNA and occupation of the minor groove by the daunosamine sugar moiety.[8] Noncovalent binding of Dox to DNA is, however, readily reversible, and noncovalent complexes have relatively short half-lives ($t_{1/2}$ ∼ minutes). Nonetheless, in clinical trials noncovalent association of Dox with calf-thymus DNA reduced

Received: November 25, 2013
Revised: January 22, 2014

Dox cardiotoxicity and improved the therapeutic index.[9] Dox also forms covalent adducts with DNA that are more stable but require an aldehyde precursor to link the daunosamine sugar of Dox to the exocyclic amine of guanine with the reaction proceeding via a Schiff base intermediate.[10,11] Dox−DNA covalent adducts are more cyotoxic than noncovalent complexes, and covalent adducts have been synthesized and used as end-points in studies of anthracycline cytotoxicity.[12] Formaldehyde is used in the formation of Dox−DNA adducts, and exogenous formaldehyde promotes Dox covalent adduct formation to genomic DNA. Dox−formaldehyde conjugates have been prepared and used for delivery of an activated form of Dox that favors covalent adduct formation to genomic DNA.[13]

We describe here the synthesis of a covalent conjugate of Dox to a single site of a DNA hairpin and demonstrate that this conjugate can be targeted to breast cancer cells. Dox covalent binding to DNA occurs primarily at N2 of guanines with sequence specificity for 5′-dGpC sites, suggesting a 3D conformation that facilitates covalent binding.[14] Our studies utilized a 25mer DNA hairpin that included a GAA hairpin-promoting sequence closed by a CG base pair with the stem consisting of 10 dA-dT base pairs (Figure 1). Although the hairpin included two dG sites, using 2D NMR in conjunction with site-specific labeling we determined only G15 in the GAA hairpin promoting motif formed a covalent adduct with Dox (Figure 2). Molecular modeling suggested that G15 N2 was not engaged in alternative interactions stabilizing the hairpin and that the tetracene ring system intercalated between the CG and first AT base pairs (Figure 3). The Dox-conjugated hairpin was exceedingly stable with a half-life of ∼30 h at physiological pH while the noncovalent complex had a half-life of minutes (Figure 4). Dox was however efficiently released at the acidic pH of endosomes following cell uptake (Figure 5). Folic acid conjugation of the hairpin resulted in cell-specific uptake into breast cancer cells and selective cytotoxicity toward targeted cells (Figure 6). These results demonstrate the utility of DNA hairpin conjugates for the improved delivery of Dox and other anticancer drugs.

■ EXPERIMENTAL SECTION

Materials. All nonlabeled hairpin DNA sequences were synthesized by IDT (Coralville, Iowa, USA). Isotopically labeled hairpins were synthesized by the DNA core lab at Wake Forest University. Clinical samples of doxorubicin (Dox) used for cell assays and DCH synthesis were obtained from the Wake Forest Baptist hospital pharmacy. Cu^{2+}-Tris[(1-benzyl-1*H*-1,2,3-triazol-4-yl)methyl]amine (Cu^{2+}-TBTA) was obtained from Lumiprobe (Hallandale Beach, Florida, USA). All media for cell culture was obtained from the Wake Forest University Cell and Viral Vector Core Lab. All other chemicals were obtained from Sigma-Aldrich and used as received.

Synthesis of DCH. A 0.37% (by weight) solution of formaldehyde was prepared by dissolving paraformaldehyde in Dulbecco's Phosphate Buffered Saline without calcium or magnesium (PBS) pH 7.4. Doxorubicin was added to 4 °C formaldehyde−PBS to obtain a final doxorubicin concentration of 250 μM. DNA hairpin loops were prepared as previously reported[6] by heating and flash-cooling of the DNA to favor intramolecular hairpin formation over dimerization. Hairpins were added to the Dox−formaldehyde solution to obtain a final hairpin concentration of 100 μM. Reactions were allowed to proceed at 10 °C in the dark for 48 h. DCHs were purified by extracting twice with phenol/chloroform and twice with chloroform. This extraction removes unreacted dox from the solution. After extraction, DCHs were ethanol-precipitated and recovered by centrifugation. Pellets were rinsed twice with 70% ethanol and 100% ethanol to remove any residual formaldehyde. Pellets were then evaporated to dryness under reduced pressure. The red−pink pellets were then resuspended in water. A Beckman Coulter DU 800 was used to measure absorption at 260 nm. Yields were typically 70−80% for the conjugate as measured by UV absorbance at 260 nm. All products were stored at −20 °C.

Synthesis of Alkyne Functionalized Folic Acid. Alkyne functionalized folic acid was synthesized similarly to previously reported methods.[15,16] Briefly, folic acid (100 mg, 0.227 mmol) was dissolved into 10 mL of DMF and stirred with a magnetic stirrer and cooled in an ice bath for 30 min before proceeding. 1-Ethyl-3-(3-dimethylaminopropyl)carbodiimide HCl (EDC) (38.7 mg, 0.249 mmol) was added to the stirred solution and allowed to react for 30 min. *N*-Hydroxysuccinimide (NHS) (31.4, 0.272 mmol) was then added to the reaction vessel and stirred for an additional 30 min. Propargyl amine (25 mg, 0.454 mmol) was then added to the reaction, which was warmed to room temperature and allowed to react for 24 h. 10 mL of 1:1 diethyl ether/chloroform was added to the reaction vessel, which precipitated the yellow−orange product. This was collected and washed three times with chloroform, diethyl ether, and water. The product was dried under vacuum overnight. Yield 69 mg (64%). ^{1}H NMR (DMSO-d_6, ppm): 11.06 (−OH), 8.64 (PteridineC$_7$ ***H***), 8.29−8.24 (−CON***H***-$CH_2C{\equiv}CH$), 8.04 (−CON***H***$CHCO_2H$), 7.67−7.65 (Ph−C_2***H*** and Ph−C_6***H***), 6.94 (−NH_2), 6.64 (Ph−C_3***H*** and Ph−C_5***H***), 4.48 (PteridineC$_6$−CH_2NH-Ph), 4.31 (−CON-HC***H***CO_2H), 3.81 (−CONH-CH_2C≡CH), 3.08 (−CONH−$CH_2C{\equiv}C$***H***), 1.98−1.96 (−C***H***CH_2CH_2), 1.87−1.85 (−$CHCH_2CH_2$, 2H).

Synthesis of FA-DCH. Hairpin with a 5′ terminal azide was used for the synthesis of FA-DCH. 45 μL of a 100 μM solution of the hairpin was added to a 500 μL centrifuge tube. To this 10 μL (pH = 7, 2 M) of triethylamine/acetic acid buffer was added and mixed. 45 μL DMSO was then added to the solution and mixed well. 4.5 μL of a 10 mM solution of alkyne functionalized folic acid was added to the solution, mixed, and bubbled with Ar for 15 min. 10 μL of 5 mM ascorbic acid in water was added to the solution followed by 5 μL of Cu^{2+}-TBTA. The reaction was mixed and bubbled with Ar for 15 min before sealing the tube and being placed in the dark at room temperature for 24 h. FA-DCH was purified similarly to DCH. The hairpin was precipitated using 4× volume ethanol and 25 μL PBS and was cooled at −20 °C for 30 min. The hairpin was recovered by centrifugation at 13 000 × *g* for 30 min. The pellet was rinsed 2× with 70% EtOH and 2× with 100% EtOH and dried under reduced pressure. The pellet was resuspended with 500 μL PBS and was dialyzed against PBS using a Slide-a-Lyzer 2 kDa MW cutoff dialysis cassette (Pierce) for 6 h to remove unreacted propargyl-folate. The retained solution was collected and quantified via UV−vis spectroscopy, with a final yield of 53%.

Doxorubicin−DNA Conjugate Ratio Measurements. DNA samples were prepared to 10 μM in dH_2O and absorbencies were measured from 200 to 800 nm using a Beckman Coulter DU800 spectrophotometer. A standard curve of Dox was established between 1 μM and 10 μM by using absorbance at 494 nm. To assess the amount of Dox covalently bound to DNA, the samples were heated to 85 °C before

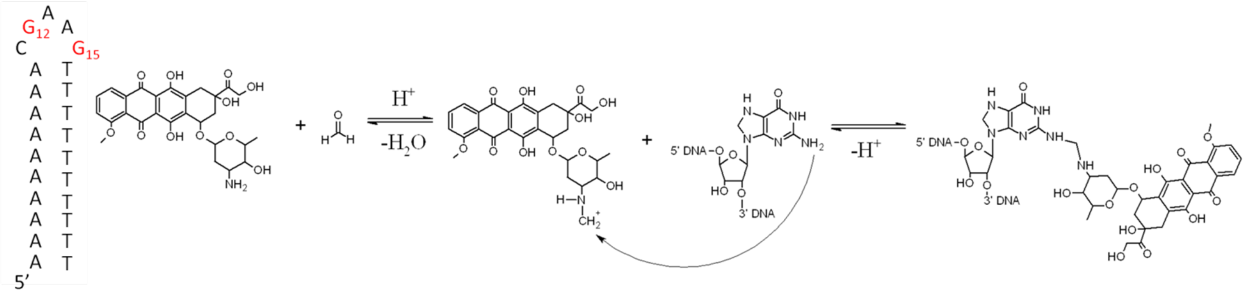

Figure 1. Reversible reaction between Doxorubicin and the exocyclic amino of Guanine in DNA mediated through formaldehyde. Red "G" in the secondary structure of the hairpin denotes potential sites of Dox reactivity.

measuring the absorbance at 494 nm. The 260 nm wavelength was used to determine the DNA content in the sample and to determine the Dox:DNA ratio.

Mass Spectrometry. Negative ion mass spectra were acquired using a Waters Q-TOF API-US mass spectrometer equipped with an Advion Nanomate source. Samples were diluted to about 5 μM with methanol/water/2-propanol (49:49:2, v:v:v). Backing pressure and sprayer voltage were optimized for each analysis, but were usually about 0.8 psi and 1.2 kV, respectively. The cone voltage was 35 V. The scan range from 525 m/z to 1600 m/z with an acquisition time of 1.2 s. Spectra were summed for 0.5 min for MaxEnt transform. The nucleotide GCATCCTGGAAAGCTACCTT, M− = 6366.1, at 0.6 μM was used to monitor instrument performance. Spectra were analyzed using MassLynx 4.0.

NMR Spectroscopy. NMR samples were prepared in 50 mM sodium phosphate buffer, pH 7.0, with 10% D_2O, and a final volume of 250 μL. All NMR spectra were acquired using a Bruker Avance 600 MHz spectrometer at 10 °C using a TXI Cryoprobe. NOESY spectra were acquired with a 100 ms mixing time and 3−9−19 Watergate water suppression with a 220 μs interpulse delay. HSQC spectra were acquired using a 110 μs 3−9−19 interpulse delay and the ^{15}N transmitter set to 150 ppm for imino groups and to 75 ppm for amino groups (indirectly referenced to water at 4.7 ppm). Data were processed using NMRPipe[17] and analyzed using NMRView.[18]

3D Modeling of DCH. A PDB file of the hairpin molecule was obtained from the Protein Data Base under entry 1JVE.[19] A PDB file of Dox was obtained from the Protein Data Base under entry DM2. Files were loaded into Pymol,[20] and the hairpin was modified to contain only 5′-ACGAAGT-3′. The models were then manipulated spatially to allow for a covalent bond to form between the N2 amino of G12 and the daunosamine of Dox. Hydrogens were added to the entire model using the Molefacture plugin vmd.[21] The doxorubicin was then geometry optimized in the presence of the DNA using PM6[22] as implemented in Gaussian 09.[23]

Dox Transfer from DCH. Samples of 2.5 μM (approximately 2 μg in 100uL) DCH, doxorubicin, or hairpin +doxorubicin were prepared in DPBS with or without a 100-fold by weight (200 μg) excess of Salmon Sperm DNA and incubated at 37 °C. Fluorescence intensity was determined by Typhoon-9210 variable mode imager with excitation set to 532 nm and the emission filter at 610 nm.

Acid Dissociation of Dox from DCH. DCH was suspended in either pH 7.4 PBS or pH 4 PBS buffer and incubated at 37 °C for 1 h. After incubation, the solutions were extracted with 2× volume phenol/chloroform and twice with 2× volume chloroform. The absorbance of the aqueous phase at 498 nm was measured. The experiment was repeated in triplicate. The results were normalized to the pH 7.4 sample with error bars representing the standard deviation of the mean of the three replicates.

Microscopy. 4T1 cells were seeded at 20 000 cells/well in 8-well Lab-Tek II chambered #1.5 German Coverglass System (Thermo Fisher Scientific, Waltham, MA), and incubated at 37 °C under 5% CO_2 for 24 h prior to treatment. Cells were incubated with 1 μM of DCH, FA-DCH, or Dox in DMEM medium with 10% dialyzed fetal bovine serum for either 1 or 4 h at 37 °C. Cells were then washed with fresh media and Dulbecco's PBS. Cells were visualized using a Zeiss LSM510 confocal microscope (Carl Zeiss, Oberkochen, Germany) using Dox as the fluorescent probe. Internalization of Dox was quantified using ImageJ software with at least 30 observations per treatment. Fluorescence intensity values were then converted to % controls using nontreated cells. The mean of the intensities was found and standard deviation was determined. Significance was determined using a two-tailed Student's t test.

Cytotoxicity. 4T1 cells were grown in DMEM media containing 10% dialyzed FBS and 1% penicillin/streptomycin, at 37 °C and 5% CO_2. 4T1 cells were plated at 5000 cell per well in 96 well plates in 100 μL media and incubated for 24 h. Cells were treated with 200 nM of either DCH, Dox, or FA-DCH for 72 h with 4 replicates of each treatment used to determine means and standard deviation. CellTiter-Glo luminescent cell viability assay (Promega) was implemented according to the manufacturer's protocol. Significance was determined using a two-tailed Student's t test.

RESULTS

Site-Specific Dox Conjugation of a DNA Hairpin. The DNA hairpin used for these studies includes two guanines (Figure 1) either of which may in principle be a site for Dox conjugation. Dox conjugates have been previously described for guanines engaged in GC base pairs; however, the chemical reactivity of the GAA sequence motif used to promote intramolecular hairpin formation has not been previously investigated. UV spectroscopy studies (Figure 2A) revealed that Dox conjugation occurred with 1:1 stoichiometry even in cases where reaction conditions permitted formation of conjugates of 2:1 or higher stoichiometry. The 1:1 stoichiometry of the conjugates was further demonstrated using ESI-QTOF mass spectrometry (Figure 2B). Mass spectrometry analysis also confirmed that the conjugation occurred via a methylene bridge derived from formaldehyde consistent with reaction proceeding via a Schiff base intermediate. To determine to what extent each of the two guanines in the hairpin were adducted in the

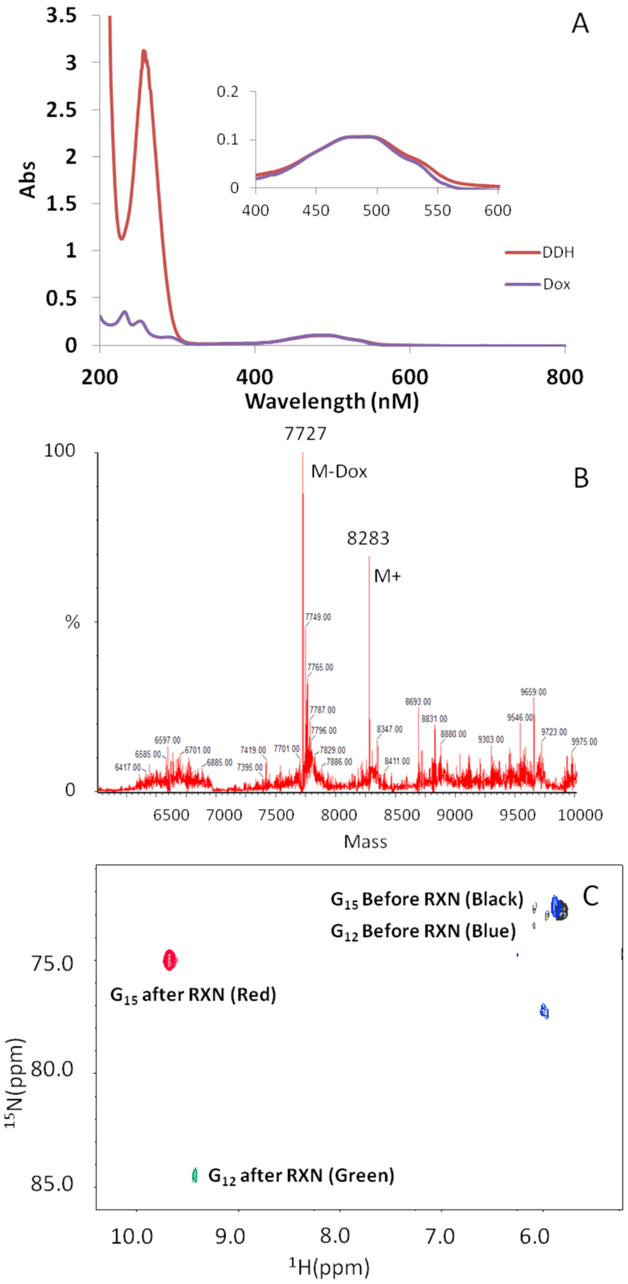

Figure 2. (A) UV−vis absorbance spectra for equmiolar amounts of Dox and DCH. Equal absorbance at 480 nm is consistent with the DCH complex being of 1:1 stoichiometry. (B) M-Dox peak of MW 7727 corresponds to the unreacted parent DNA, while the M+ peak of MW 8283 is obtained by the addition of Dox (MW 543) and CH_2 (MW 14) −2H lost as water. (C) Overlay of $^{1}H-^{15}N$ HSQC displaying the N2 of G12 and G15 from two independent singly labeled samples. Blue and green peaks represent the G12 amino before and after reaction with Dox, respectively. Black and red peaks represent the G15 amino before and after reaction, respectively.

conjugate, we synthesized the hairpin site-specifically ^{15}N-labeled at either G12 or G15 and formed Dox conjugates with both species and analyzed each for chemical adduction based on chemical shift changes in 2D [$^{1}H-^{15}N$] NMR spectra (Figure 2C). Substantial ^{15}N chemical shift changes were only detected for the hairpin labeled at G12 (72.6 → 84.5 ppm), consistent with this site selectively undergoing chemical modification upon adduct formation. This represents the first time that we are aware of that Dox covalent bonding has been observed in a hairpin loop region of DNA. G15, which is engaged in a GC base pair that closes the loop, underwent substantial change in ^{1}H (5.8 → 9.7 ppm) but not ^{15}N chemical shift (72.8 → 75.0 ppm) consistent with this site undergoing changes in chemical environment, but not chemical structure, upon Dox conjugation. Subsequent molecular modeling studies revealed the CG based pair was stacked with the tetracene ring system of Dox in the resulting conjugate (vide infra).

Molecular Model of Dox-Conjugated Hairpin. We then sought to create a working model for the structure of the Dox-conjugated hairpin (Figure 3) using the data collected from the ^{15}N-edited 2D NMR and using a NMR structure of the hairpin loop characterized by Ulyanov et al.[19] as the starting point for model development. The hydrogen shifts of G15 could be caused by intercalation of Dox in the covalent complex, as shifts of amino protons to ∼10 ppm have been attributed to increased hydrogen bonding in quadruplex DNA.[24] Preliminary data also showed that the amino of G15 displayed several NOEs consistent with Dox localizing in the stem region of the hairpin (SI 1). Pymol was used to edit the DNA from the previous NMR structure to contain only the loop region and the first AT base pair. We then manipulated a model of Dox into a position that brought the amino hydrogens of G12 and Dox into close proximity, allowing for the formation of a methylene bridge between the amino nitrogens. This placement also allowed Dox to intercalate between the C11-G15 base pair and the first AT base pair in the stem of the DNA (Figure 3A,B). Modeling revealed that the simultaneous covalent binding at G12 and intercalation of Dox between the A10:T16 and C11:G15 occurred with minimal distortion to the structure of the hairpin loop (Figure 3C,D). The daunosamine sugar is of appropriate dimensions to span the distance between the sites of covalent binding and intercalation and the amino group of G12 is not engaged in hydrogen

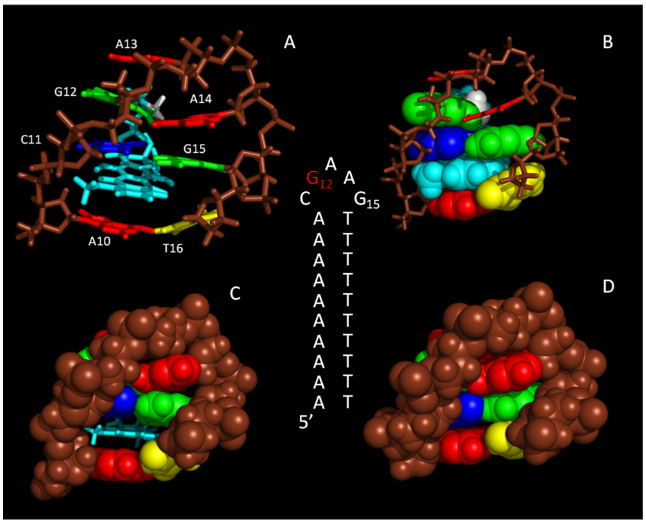

Figure 3. Secondary structure and molecular model of the DCH. Dox is bound to N2 of G12 and intercalated between the G15:C11 and A10:T16 base pairs. The lower 9 AT base pairs of the stem have been truncated for simplicity. Structures are colored as follows: guanine, green; adenine, red; thymine, yellow; cytosine, blue; Dox, light blue; methylene linker, white; DNA backbone, brown. (A−C) 3D modeling of the DCH structure. (D) 3D model of the unreacted hairpin.

bonding interactions that contribute significantly to the structure and stability of the hairpin loop. Intercalation of the tetracene ring alters local base stacking for the proximal base pairs but does not disrupt hydrogen bonding interactions (Figure 3D).

Stability of Dox–Hairpin Conjugate. We hypothesized that covalent binding of Dox would allow for the Dox-conjugated hairpin to serve as a delivery vehicle with improved pharmacological properties and reduced systemic toxicities relative to conventional Dox. In order for the hairpin to act as an efficient delivery vehicle, Dox must remain stably bound under physiological conditions, but also undergo intracellular release and transfer to genomic DNA. Interestingly, Dox retains most of its fluorescent activity in the hairpin, but not in larger DNA molecules which are known to quench the fluorescence of the drug[26] (SI 2). We hypothesized that as the Dox–hairpin bond is hydrolyzed, the free Dox could intercalate into larger DNA molecules, quenching the fluorescence. Using the difference in fluorescence between hairpin bound Dox and Dox intercalated into DNA, we can measure the half-life of the Dox–hairpin bond. We developed an assay to quantify the transfer of Dox from the hairpin to genomic DNA under physiologic conditions. This assay is based on the difference in fluorescence of Dox in the context of the hairpin conjugate relative to genomic DNA. The hairpin conjugate, free-Dox, or the noncovalent complex (e.g., hairpin+Dox) were mixed with 100-fold excess of salmon sperm DNA (spDNA; w/w) to simulate genomic DNA. Reactions were incubated at 37 °C with fluorescence quenching measured over 48 h. No fluorescence loss was observed in samples that lacked spDNA, while fluorescence was fully quenched within one hour following addition of spDNA for both free Dox and the noncovalent complex. The rate of loss of fluorescence quenching was, however, significantly reduced for the hairpin conjugate with 50% quenching occurring at 30.4 h (Figure 4). Using $t_{1/2}$ of 30.4 h and assuming zero-order kinetics, the rate constant is 1.15^{-11} M/s. Given that the noncovalent hairpin +Dox complex undergoes rapid quenching, intercalation into the hairpin cannot be solely responsible for the increased chemical stability of the hairpin conjugate. Covalent Dox dimers formed using formaldehyde have been shown to be readily hydrolyzable under physiological conditions, resulting in complete disassociation of Dox and formaldehyde release within ~15 min.[13] Thus, it is likely that a combination of both intercalation and covalent bonding is responsible for the substantially increased stability for the Dox-conjugated hairpin relative to the noncovalent complex and alternative Dox covalent complexes. We hypothesize that the covalent linkage acts as a tether between the Dox and DNA, and that when the bond is hydrolyzed, intercalation holds the resulting amine and Schiff-base in close proximity allowing for them to reform the covalent linkage. At physiological pH, equilibrium favors reforming the covalent complex, while at acidic pH, for example, in endosomes, equilibrium disfavors reforming the covalent linkage and instead results in release of Dox from the intercalated complex.

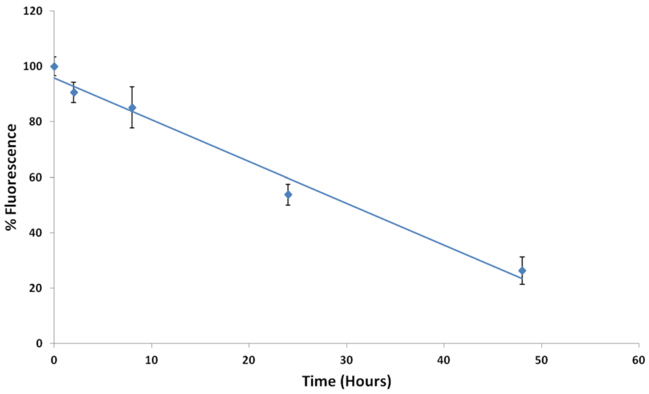

Figure 4. Fluorescence quenching of DCH displays a ~50% reduction in fluorescence after 30 h, while noncovalent complexes display greater than 50% reduction in fluorescence within 1 h (data not shown). Error bars represent standard deviation of the mean of three measurements. Assuming zero-order kinetics, the rate constant is $k = 1.15 \times 10^{-11}$ M/s.

Targeted Uptake and Enhanced Cytotoxicity to Breast Cancer Cells. Cellular uptake of exogenous DNA can be highly efficient if uptake occurs via receptor-mediated processes. Our initial studies with the Dox-conjugated hairpin indicated uptake into breast cancer cells was less efficient than for F10, a single-stranded DNA investigated in our previous studies. As our previous studies demonstrated that conjugation with folic acid improved F10 uptake into drug-resistant colon cancer cells,[25] we investigated whether conjugating the Dox-hairpin at the 5′-terminus with folic acid would improve uptake into 4T1 breast cancer cells. Folic acid conjugation of the hairpin resulted in significantly increased cellular uptake relative to the nonconjugated hairpin based upon increased Dox fluorescence into 4T1 breast cancer cells (Figure 5). Dox fluorescence was initially localized in endosomes (SI 3) consistent with cellular internalization via an endocytic process and with release of Dox at the acidic pH of endosomes. Folic acid conjugation also increased the cytotoxicity of the Dox-conjugated hairpin toward 4T1 cells consistent with both improved cell uptake and efficient Dox release (Figure 6). The results demonstrate that, while the Dox-conjugated hairpin has markedly improved stability at physiological pH relative to the corresponding noncovalent complex, the conjugate is highly effective at the intracellular release of Dox following cell uptake.

■ DISCUSSION

DNA is central to biology as the predominant carrier of genetic information; however, the physical and chemical properties of DNA make it highly useful as a material for numerous applications including use for drug delivery. These studies have demonstrated that a simple DNA hairpin that includes a "GAA" hairpin-promoting sequence provides a unique site for conjugation with the Top2-poisoning anticancer drug Dox. Conjugation occurs without disrupting stabilizing hydrogen bonding or base stacking interactions in the hairpin loop and allows for facile intercalation of the tetracene ring system of Dox between the first and second base pairs of the hairpin stem. The concurrent covalent linkage and intercalation of Dox in the hairpin results in formation of a complex that is highly stable at physiological pH. As noncovalent Dox–DNA complexes, presumably of greatly reduced chemical stability relative to the Dox-conjugated DNA hairpin described here have shown decreased toxicity relative to free Dox in human clinical trials,[9] hairpin conjugates may represent an improved approach for limiting Dox toxicity while preserving Dox efficacy.

A number of approaches have been described for improved Dox delivery while limiting systemic toxicities. The liposomal formulation Doxil, for example, has demonstrated clinical

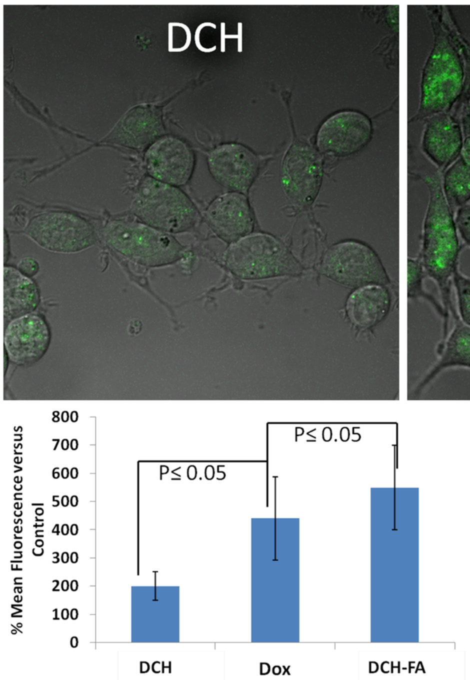

Figure 5. (A) Fluorescence microscopy of 4T1 cells treated with either untargeted or folate-targeted DCH. (B) Quantification of Dox fluorescence from 4T1 cells. Error bars represent standard deviation from the mean of at least 30 measurements. A Student's two-tailed *t* test was used to determine significance.

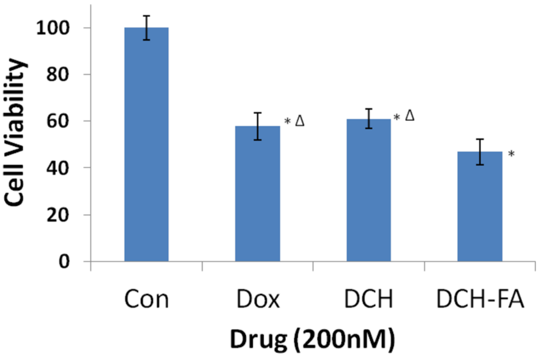

Figure 6. Targeting DCH with folic acid (DCH-FA) significantly increases the cytotoxicity of the DCH construct toward 4T1 breast cancer cells. Error bars represent standard deviation from the mean with four replicates of each condition. A Student's two-tailed *t* test was used to determine significance (i.e., $p < 0.05$)— *significantly different from control; $^{\Delta}$significantly different from DCH-FA.

utility.[27] A variety of other nanoparticle-mediated drug delivery approaches have also been explored for improved Dox delivery.[28−30] DNA offers many advantages relative to alternative strategies. DNA is readily biodegradable and can be used for in vivo applications without activating an immune response. Further, the use of DNA for drug delivery allows for natural combination of diverse anticancer drugs of different classes. For example, our laboratory has pioneered the inclusion of cytotoxic nucleotide analogs into ssDNA[4,5] and more recently into DNA hairpins.[6,7] We have also shown that duplex or hairpin DNA can be used for delivery of minor groove binding ligands.[6,7] The present studies have extended this work to include covalent modification of DNA hairpins with simultaneous intercalation by DNA-targeting drugs, such as the Top2 poison Dox. Our studies have also shown that the major groove of DNA can be used for improved drug delivery as our studies have shown that Zn^{2+} complexation occurs in the major groove of FdU-substituted DNA hairpins.

Drug delivery is a multifaceted process that involves not only improved stability in circulation, but also specific uptake into targeted cells and ultimately release of drug following cell uptake. Our studies show that, as with previous studies with the single-stranded DNA F10, conjugation with folic acid improves uptake into targeted cancer cells.[25] Many cancer cells overexpress folate receptor as a consequence of increased nutrient requirements to support an elevated growth rate for the malignant phenotype.[31] These studies show cell uptake of a 25 nucleotide DNA hairpin can be significantly enhanced into 4T1 breast cancer cells through folic acid conjugation. Importantly, while the Dox-conjugated hairpin is highly stable at physiological pH, Dox release is favored at the acidic pH of endosomes following cell uptake. Dox is efficiently released from the hairpin following cell uptake and Dox retains potency as an anticancer drug. The results demonstrate that the DNA-conjugation strategy developed has the requisite components to be useful for Dox delivery in a clinical setting.

To our knowledge, this is the first report of the use of a Dox−DNA covalent conjugate to transfer Dox to DNA for potential therapeutic applications. The approach adopted has potential for greatly expanded drug delivery applications. For example, we have previously shown that FdU nucleotides can be embedded within this hairpin sequence and that the resulting hairpin is cytotoxic to prostate cancer cells.[6,7] As DNA polymers containing FdU nucleotides are Top1 poisons, the present system allows for creating complexes that deliver both FdU and Dox and that will simultaneously target Top1 and Top2. Simultaneous targeting of Top1 and Top2 has shown promise for clinical management of cancer, although this combination displays systemic toxicities.[32,33] Our studies show that folic acid conjugation can be used to improve uptake for DNA hairpin conjugates into breast cancer cells, and this is expected to concomitantly reduce systemic toxicities. Studies are underway to evaluate these promising concepts in drug delivery. Future studies will focus on demonstrating advantages in cellular and animal models of cancer.

CONCLUSIONS

The "GAA" sequence motif that promotes intramolecular DNA hairpin formation can be selectively conjugated to the Top2-poisoning anticancer drug Dox. The resulting conjugate is highly stable at physiological pH as a consequence of both covalent modification and intercalation of the tetracene ring system of Dox into the hairpin stem. Folic acid conjugation of the Dox-conjugated hairpin enhances uptake by 4T1 breast cancer cells. Dox is efficiently released at the acidic pH of endosomes following cell uptake demonstrating that the Dox-conjugated hairpin has both appropriate extracellular stability and intracellular lability well-suited for drug delivery applications. The DNA hairpin structural motif permits further development by inclusion of additional or alternative cytotoxic drugs, such as FdU or other cytotoxic nucleotide analogs demonstrating the multifunctional properties of DNA as a material for drug delivery science.

ASSOCIATED CONTENT

Ⓢ Supporting Information

NOESY NMR spectra of DCH, absorbance of DCH after acid extractions, and fluorescence microscopy of Dox endosomal uptake by 4T1 cells. This material is available free of charge via the Internet at http://pubs.acs.org/.

AUTHOR INFORMATION

Corresponding Author

*Phone: (336) 716-6216. Fax: (336) 716-0255. E-mail: bgmeiner@wakehealth.edu.

Present Address

[⊥]David A. Horita, University of North Carolina Nutrition Research Institute, Kannapolis, NC 28081.

Notes

The authors declare no competing financial interest.

ACKNOWLEDGMENTS

The authors would like to thank Michael Samuel from the Wake Forest University Mass Spectrometry Core Lab for his help in obtaining all of the mass spectrometry data used in this research. Oligonucleotide syntheses were performed in the DNA Synthesis Core Laboratory at Wake Forest University School of Medicine. The DNA Synthesis and the Mass Spectrometry Cores are part of the Bioanalytical Core Laboratory supported in part by the Comprehensive Cancer Center of Wake Forest University. Funding was provided by Department of Defense Prostate Cancer Research Program (093606 to W.H.G.) and the Comprehensive Cancer Center of Wake Forest University Cancer Center Support Grant P30 CA012197 supporting the Bioanalytical Core Laboratory. The Waters Q-TOF mass spectrometer was purchased with funds from NIH Shared Instrumentation Grant 1S10RR17846. MS analyses were performed in the Mass Spectrometer Facility of the Comprehensive Cancer Center of Wake Forest University School of Medicine supported in part by NCI center grant 5P30CA12197.

REFERENCES

(1) Elliott, P. (2006) Pathogenesis of cardiotoxicity induced by anthracyclines. *Semin. Oncol. 33* (3Suppl8), S2–7.

(2) Sordet, O., Khan, Q. A., Kohn, K. W., and Pommier, Y. (2003) Apoptosis Induced by Topoisomerase Inhibitors. *Curr. Med. Chem. Anti-Cancer Agents 3*, 271–290.

(3) Zhang, S., Liu, X., Bawa-Khalfe, T., Lu, L.-S., Lyu, Y. L., Liu, L. F., and Yeh, E. T. H. (2012) Identification of the molecular basis of doxorubicin-induced cardiotoxicity. *Nat. Med. 18*, 1639–1642.

(4) Liao, Z.-Y., Sordet, O., Zhang, H.-L., Kohlhagen, G., Antony, S., Gmeiner, W. H., and Pommier, Y. (2005) A novel polypyrimidine antitumor agent FdUMP[10] induces thymineless death with topoisomerase I-DNA complexes. *Cancer Res. 65*, 4844–4851.

(5) Pardee, T. S., Gomes, E., Jennings-Gee, J., Caudell, D., and Gmeiner, W. H. (2012) Unique dual targeting of thymidylate synthase and topoisomerase1 by FdUMP[10] results in high efficacy against AML and low toxicity. *Blood 119*, 3561–3570.

(6) Ghosh, S., Salsbury, F. R., Jr., Horita, D. A., and Gmeiner, W. H. (2011) Zn2+ selectively stabilizes FdU-substituted DNA through a unique major groove binding motif. *Nucleic Acids Res. 39*, 4490–4498.

(7) Ghosh, S., Salsbury, F. R., Jr., Horita, D. A., and Gmeiner, W. H. (2013) Cooperative stabilization of Zn(2+):DNA complexes through netropsin binding in the minor groove of FdU-substituted DNA. *J. Biomol. Struct. Dyn. 31*, 1301–1310.

(8) Wang, A. H., Gao, Y. G., Liaw, Y. C., and Li, Y. K. (1991) Formaldehyde cross-links daunorubicin and DNA efficiently: HPLC and X-ray diffraction studies. *Biochemistry 30*, 3812–3815.

(9) Trouet, A., and Jolles, G. (1984) Targeting of daunorubicin by association With DNA or proteins: a review. *Semin. Oncol. 11* (4Suppl3), 64–72.

(10) Zeman, S. M., Phillips, D. R., and Crothers, D. M. (1998) Characterization of covalent Adriamycin-DNA adducts. *Proc. Natl. Acad. Sci. U.S.A. 95*, 11561–11565.

(11) Cutts, S. M., Parker, B. S., Swift, L. P., Kimura, K. I., and Phillips, D. R. (2000) Structural requirements for the formation of anthracycline-DNA adducts. *Anti-Cancer Drug Des. 15*, 373–386.

(12) Swift, L. P., Cutts, S. M., Rephaeli, A., Nudelman, A., and Phillips, D. R. (2003) Activation of adriamycin by the pH-dependent formaldehyde-releasing prodrug hexamethylenetetramine. *Mol. Cancer Ther. 2*, 189–198.

(13) Post, G. C., Barthel, B. L., Burkhart, D. J., Hagadorn, J. R., and Koch, T. H. (2005) Doxazolidine, a proposed active metabolite of doxorubicin that cross-links DNA. *J. Med. Chem. 48*, 7648–7657.

(14) Phillips, D. R., White, R. J., and Cullinane, C. (1989) DNA sequence-specific adducts of adriamycin and mitomycin C. *FEBS Lett. 246*, 233–240.

(15) Lee, R. J., and Low, P. S. (1994) Delivery of liposomes into cultured KB cells via folate receptor-mediated endocytosis. *J. Biol. Chem. 269*, 3198–3204.

(16) Zhang, H., Cai, Z., Sun, Y., Yu, F., Chen, Y., and Sun, B. (2012) Folate-conjugated β-cyclodextrin from click chemistry strategy and for tumor-targeted drug delivery. *J. Biomed. Mater. Res. A 100*, 2441–2449.

(17) Piotto, M., Saudek, V., and Sklenár, V. (1992) Gradient-tailored excitation for single-quantum NMR spectroscopy of aqueous solutions. *J. Biomol. NMR 2*, 661–665.

(18) Delaglio, F., Grzesiek, S., Vuister, G. W., Zhu, G., Pfeifer, J., and Bax, A. (1995) NMRPipe: a multidimensional spectral processing system based on UNIX pipes. *J. Biomol. NMR 6*, 277–293.

(19) Ulyanov, N. B., Bauer, W. R., and James, T. L. (2002) High-resolution NMR structure of an AT-rich DNA sequence. *J. Biomol. NMR 22*, 265–280.

(20) *The PyMOL Molecular Graphics System*, v 1.5.0.4; Schrödinger, LLC.

(21) Humphrey, W., Dalke, A., and Schulten, K. (1996) VMD: visual molecular dynamics. *J. Mol. Graphics 14*, 33–38.

(22) Stewart, J. J. P. (2007) Optimization of parameters for semiempirical methods V: Modification of NDDO approximations and application to 70 elements. *J. Mol. Model. 13*, 1173–1213.

(23) Frisch, M. J., Trucks, G. W., Schlegel, H. B., Scuseria, G. E., Robb, M. A., Cheeseman, J. R., Scalmani, G., Barone, V., Mennucci, B., Petersson, G. A., Nakatsuji, H., Caricato, M., Li, X., Hratchian, H. P., Izmaylov, A. F., Bloino, J., Zheng, G., Sonnenberg, J. L., Hada, M., Ehara, M., Toyota, K., Fukuda, R., Hasegawa, J., Ishida, M., Nakajima, T., Honda, Y., Kitao, O., Nakai, H., Vreven, T., Montgomery, Jr., J. A., Peralta, J. E., Ogliaro, F., Bearpark, M., Heyd, J. J., Brothers, E., Kudin, K. N., Staroverov, V. N., Kobayashi, R., Normand, J., Raghavachari, K., Rendell, A., Burant, J. C., Iyengar, S. S., Tomasi, J., Cossi, M., Rega, N., Millam, J. M., Klene, M., Knox, J. E., Cross, J. B., Bakken, V., Adamo, C., Jaramillo, J., Gomperts, R., Stratmann, R. E., Yazyev, O., Austin, A. J., Cammi, R., Pomelli, C., Ochterski, J. W., Martin, R. L., Morokuma, K., Zakrzewski, V. G., Voth, G. A., Salvador, P., Dannenberg, J. J., Dapprich, S., Daniels, A. D., Farkas, Ö., Foresman, J. B., Ortiz, J. V., Cioslowski, J., and Fox, D. J. (2009) *Gaussian 09*, rev A.1, Gaussian, Inc., Wallingford, CT.

(24) Bouaziz, S., Kettani, A., and Patel, D. J. (1998) A K cation-induced conformational switch within a loop spanning segment of a DNA quadruplex containing G-G-G-C repeats. *J. Mol. Biol. 282*, 637–652.

(25) Liu, J., Kolar, C., Lawson, T. A., and Gmeiner, W. H. (2001) Targeted drug delivery to chemoresistant cells: folic acid derivatization of FdUMP[10] enhances cytotoxicity toward 5-FU-resistant human colorectal tumor cells. *J. Org. Chem. 66*, 5655–5663.

(26) Bagalkot, V., Lee, I.-H., Yu, M. K., Lee, E., Park, S., Lee, J.-H., and Jon, S. (2009) A combined chemoimmunotherapy approach using a plasmid-doxorubicin complex. *Mol. Pharmaceutics 6*, 1019–1028.

(27) O'Brien, M. E. R., Wigler, N., Inbar, M., Rosso, R., Grischke, E., Santoro, A., Catane, R., Kieback, D. G., Tomczak, P., Ackland, S. P., Orlandi, F., Mellars, L., Alland, L., Tendler, C., et al. (2004) Reduced cardiotoxicity and comparable efficacy in a phase III trial of pegylated liposomal doxorubicin HCl (CAELYX/Doxil) versus conventional doxorubicin for first-line treatment of metastatic breast cancer. *Ann. Oncol. 15*, 440–449.

(28) Boyacioglu, O., Stuart, C. H., Kulik, G., and Gmeiner, W. H. (2013) Dimeric DNA aptamer complexes for high-capacity–targeted drug delivery using pH-sensitive covalent linkages. *Mol. Ther. Nucleic Acids 2*, e107.

(29) Janes, K. A., Fresneau, M. P., Marazuela, A., Fabra, A., and Alonso, M. J. (2001) Chitosan nanoparticles as delivery systems for doxorubicin. *J. Controlled Release 73*, 255–267.

(30) Chang, Y., Liu, N., Chen, L., Meng, X., Liu, Y., Li, Y., and Wang, J. (2012) Synthesis and characterization of DOX-conjugated dendrimer-modified magnetic iron oxide conjugates for magnetic resonance imaging, targeting, and drug delivery. *J. Mater. Chem. 22*, 9594.

(31) Russell-Jones, G., McTavish, K., McEwan, J., Rice, J., and Nowotnik, D. (2004) Vitamin-mediated targeting as a potential mechanism to increase drug uptake by tumours. *J. Inorg. Biochem. 98*, 1625–1633.

(32) Eder, J. P., Chan, V., Wong, J., Wong, Y. W., Ara, G., Northey, D., Rizvi, N., and Teicher, B. A. (1998) Sequence effect of irinotecan (CPT-11) and topoisomerase II inhibitors in vivo. *Cancer Chemother. Pharmacol. 42*, 327–335.

(33) Morgensztern, D., Baggstrom, M. Q., Pillot, G., Tan, B., Fracasso, P., Suresh, R., Wildi, J., and Govindan, R. (2009) A phase I study of pegylated liposomal doxorubicin and irinotecan in patients with solid tumors. *Chemotherapy 55*, 441–445.